Rotational dynamics-based assessment of energy transfer efficiency of hetero-FRET probes in crowded environments

A Thesis
SUBMITTED TO THE FACULTY OF
UNIVERSITY OF MINNESOTA
BY

Hannah J. Leopold

IN PARTIAL FULFILLMENT OF THE REQUIREMENTS
FOR THE DEGREE OF
MASTER OF SCIENCE

Dr. Erin D. Sheets

August 2017

Acknowledgements

I would like to acknowledge Dr. Arnold J. Boersma for providing us the resources to pursue this project. I would also like to acknowledge the financial support provided by the University of Minnesota Grant-in-Aid, the Minnesota Supercomputing Institute, the Chancellor's Small Grant, the Department of Chemistry and Biochemistry, and the Swenson College of Science and Engineering, all of which are from the University of Minnesota Duluth. I would like to recognize the personal financial support provided by the John C. Cothran and Moses Passer Fellowship.

I would like to express my sincerest gratitude to Dr. Erin Sheets for her friendship and mentorship throughout my time at UMD. You pushed me out of my comfort zone when I needed it most and encouraged me to not settle for anything but the best. I admire your strength, honesty, and dedication to science. I would also like to extend a true thank you to Dr. Ahmed Heikal for his undeniable kindness, intellectual curiosity, and great sense of humor. I hope someday I can give to others as much as you have given to me. I would like to thank the members of my committee, Dr. Jacob Wainman and Dr. Alessandro Cembran for their patience and support along the way.

I would also like to acknowledge the work of former graduate student, Megan Currie. This project would not be where it is today without her. Megan contributed a significant amount of knowledge and hard work to establish this project and has been a great mentor and friend. Her legacy will live on in lab and on the soccer field. I would like to thank Jacob Schwarz for not only being a great colleague but a great friend. You've humored me in my crazy science rants, perfectionist ways, and most of all; you've kept me smiling the whole way. To that, I am forever grateful. I would like to thank all of the faculty and staff in the Department of Chemistry and Biochemistry. The great people I've met and the opportunities I've been provided will not be forgotten. Last but not least, I would like to thank my family for keeping me grounded and providing me unwavering support throughout my studies and life. You made this possible and reminded me to stop and enjoy the ride along the way.

Dedication

To Taryn, who got me through all the tough bits.

Abstract

A living cell is crowded with various organelles, DNA, and proteins. Such macromolecular crowding has a significant impact on cellular processes. Yet, the effects of macromolecular crowding on protein diffusion, reaction rates, and folding are far from understood. As a result, there is a need to quantify crowding in a heterogeneous environment both *in vivo* and *in vitro*. Recently, a series of novel genetically encoded FRET probes were developed as sensors to quantitatively measure crowding *in vivo* and were characterized with steady-state fluorescence (Nat Meth [2015] 12:227). In a crowded environment, these FRET probes are hypothesized to become confined and more compact, thereby leading to enhanced energy transfer. Consequently, the level of crowding can be quantified based on the energy transfer efficiency of the probes. In this Thesis, we develop a theoretical model based on time-resolved anisotropy to quantify the FRET efficiency of the probes. Additionally, we investigate the conformational dynamics and rotational diffusion of the probes using time-resolved fluorescence anisotropy in homogeneous and heterogeneous environments. Here, we used Ficoll-70 as a heterogeneous crowder to investigate the excluded volume effects on the probes. Measurements in glycerol-enriched buffer were also conducted to distinguish between viscosity and excluded volume effects. Our results indicate that time-resolved anisotropy can be combined with these novel FRET probes for quantitative, non-invasive analysis of site-specific crowding.

Table of Contents

List of Tables ..... vii.

List of Figures ..... viii.

List of Abbreviations ..... x.

List of Symbols ..... xi.

Chapter 1: Introduction

1.1 Overview 1

1.2 Living cells are crowded with macromolecules 1

1.3 Role of macromolecular crowding 2

1.4 Theory and experimental studies of cellular crowding 2

1.5 The need for crowding sensors: a family of FRET-based crowding sensors 3

1.6 Quantitative, non-invasive methods for investigating in vitro macromolecular crowding 6

Chapter 2: Materials and methods

2.1 Overview 7

2.2 Materials and methods of FRET probe purification 7

2.3 Materials and methods of biomimetic crowding 10

2.4 Materials and methods of time-resolved anisotropy 10

2.4.1 Theory of time-resolved anisotropy 10

2.4.2 Experimental setup and calibration 12

2.4.3 Data analysis 14

Chapter 3: Theoretical model of hetero-FRET using time-resolved anisotropy

3.1 Background 17

3.2 Results and discussion 17

3.2.1 Kinetic model of anisotropy in the presence of FRET-based depolarization 17

3.2.2 Simulation and theoretical prediction 19

Chapter 4: Rotational dynamics of FRET probes in homogenous environments

4.1 Background 22

4.2 Results and Discussion 23

4.2.1 Wavelength dependence of rotational dynamics in PBS 23

4.2.2 Wavelength-dependence of FRET probes rotational dynamics in glycerol-enriched PBS 29

4.2.3 Effects of homogenous viscosity on the rotational diffusion coefficient of the FRET probes 32

4.2.4 Determining the hydrodynamic volume of the FRET probes using steady-state and time-resolved anisotropy 35

Chapter 5: Rotational dynamics of confined FRET probes in crowded environment (Ficoll-70)

5.1 Background 39

5.2 Results and discussion 39

5.2.1 Rotational dynamics of FRET probes in heterogeneous viscosity 39

5.2.2 Effects of heterogeneous viscosity on the rotational diffusion coefficient of the FRET probes 43

5.2.3 Effects of heterogeneous viscosity on the Perrin-Weber equation 44

Chapter 6: Conclusions and future directions**.....46**

References **.....48**

Appendices**.....53**

List of Tables

Table 1.1 Detailed characteristics of the linkers 4

Table 4.1 Fitting parameters of time-resolved anisotropy of intact and cleaved E6 in PBS 26

Table 4.2 Fitting parameters of time-resolved anisotropy of all probes in PBS 28

Table 4.3 Fitting parameters of time-resolved anisotropy of intact and cleaved E6 in glycerol-enriched buffers (0–760 g/L) 31

Table 4.4 Hydrodynamic volume of cleaved and intact probes under 425 nm excitation and 475/50 detection 35

Table 4.5 Hydrodynamic volume of cleaved and intact probes under 425 nm excitation and 531/40 detection 38

Table 5.1 Fitting parameters of time-resolved anisotropy of intact and cleaved E6 in Ficoll-70-enriched buffers (0–300 g/L) 41

Table A2.1 Bulk viscosity measurements of glycerol and Ficoll-70 54

Table A3.1 Förster distance of GE probe 55

Table A3.2 FRET efficiencies of all probes based on fluorescence lifetime 56

List of Figures

Figure 1.1 Structure of the five FRET probe variants 5

Figure 2.1 The absorption spectrum of the GE probe and emission spectra of the donor (mCeulean3) and acceptor (mCitrine) 9

Figure 2.2 Schematic representation of the theory of time-resolved anisotropy 11

Figure 2.3 Schematic of depolarization due to rotation and FRET 11

Figure 2.4 Schematic representation of the time-resolved fluorescence anisotropy system 13

Figure 3.1 Simulated anisotropy decay based on theoretical model.....20

Figure 4.1 Time-resolved anisotropy of intact and cleaved E6 as a function of wavelength in PBS 25

Figure 4.2 Time-resolved anisotropy of all probes in PBS and the FRET efficiency of all probes in PBS as a function of linker length 27

Figure 4.3 Time-resolved anisotropy of intact and cleaved E6 in glycerol-enriched buffer. FRET efficiency of all probes as a function of homogeneous viscosity 30

Figure 4.4 Average donor-acceptor distance of all probes as a function of homogenous viscosity.....32

Figure 4.5 Rotational diffusion of intact and cleaved GE in homogenous viscosity. Rotational diffusion of all probes in homogenous viscosity 34

Figure 4.6 Perrin-Weber plot of intact and cleaved G12 in homogenous viscosity 37

Figure 5.1 Time-resolved anisotropy of intact and cleaved E6 in Ficoll-70. FRET efficiency of all probes as a function of heterogeneous viscosity 40

Figure 5.2 Average donor-acceptor distance of all probes as a function of heterogeneous viscosity 42

Figure 5.3 Rotational diffusion of intact and cleaved GE in heterogeneous viscosity 43

Figure 5.4 Perrin-Weber plot of intact and cleaved G12 in heterogeneous viscosity 45

Figure A1.1 Representative SDS-PAGE gel of purified E6G2 and G12 53

Figure A1.2 Representative SDS-PAGE gel of intact and cleaved GE.....53

Figure A2.1 Bulk viscosity of glycerol and Ficoll-70 as a function of concentration...54

Figure A3.1 Anisotropy decay of recombinant CFP compared to cleaved probe 56

List of Abbreviations

AMP	Amplifier
cP	Centipoise
DM	Dichroic mirror
EDTA	Ethylenediaminetetraacetic acid
F	Filter
FRET	Förster resonance energy transfer
FWHM	Full width half max
G-Factor	Geometrical factor
IDP	Intrinsically disordered protein
IPTG	Isopropyl β-D-thiogalactopyranoside
L	Lens
LB	Luria Bertani
MA	Magic angle
PBS	Phosphate-buffered saline
PMSF	Phenylmethylsulfonyl fluoride
PD	Fast photodiode
RhG110	Rhodamine green, hydrochloride (5(6)-CR 110, SE)
SDS-PAGE	Sodium dodecyl sulfate-polyacrylamide gel electrophoresis
TB	Terrific broth
TCSPC	Time-correlated single-photon counting

List of Symbols

D_R	Rotational diffusion rate
E	Efficiency of energy transfer
f_i	Fractional population
G	Anisotropy geometrical factor
h	Protein hydration
$I_{\parallel}$	Parallel polarized fluorescence intensity
$I_{\perp}$	Perpendicular polarized fluorescence intensity
k_B	Boltzmann constant
k_{ET}	Energy transfer rate
k_{fl}	Rate of fluorescence
p	Polarization
$r_i(t)$	Time-resolved anisotropy
r_{ss}	Steady-state anisotropy
r_0	Initial anisotropy
R_{DA}	Average donor-acceptor distance
R_0	Förster distance at which energy transfer efficiency is 50%
t	Time
T	Temperature
v_0	Specific volume
V_i	Hydrodynamic volume
α_i	Amplitude of lifetime decay
β_i	Amplitude of anisotropy decay
θ	Angle between absorbing and emitting dipoles
κ^2	Orientation parameter between donor-acceptor dipole moments
λ	Wavelength
η	Viscosity

τ_D	Fluorescence lifetime of the donor alone
τ_{DA}	Fluorescence lifetime of the donor in the presence of the acceptor
τ_i	Fluorescence lifetime
φ_i	Rotational time
χ^2	Chi squared

Chapter 1
Introduction

1.1 Overview

A living cell is crowded with various organelles, DNA, and proteins. Such macromolecular crowding has a significant impact on cellular processes. Yet, the effects of macromolecular crowding on protein diffusion, reaction rates, and molecular folding are far from understood. In addition, it is known that crowding in living cells is compartmentalized and might be related to cell pathology. As a result, there is a need for sensitive tools to investigate the multidimensional nature of crowding. In this Thesis, the conformational dynamics and energy transfer efficiency of a new class of FRET probes is investigated using time-resolved fluorescence anisotropy as a quantitative and non-invasive approach.

1.2 Living cells are crowded with macromolecules

The idea of a cell as a simplistic structure has been continuously refuted to reveal an intricately complex and dynamic system down to the molecular level. It is now widely accepted that the interior of cells is crowded with metabolites, proteins and DNA that typically take up 20–30% of the total volume (1, 2). In 1981, Minton described the volume excluded by one molecule to another as ‘macromolecular crowding’ (3). This nonspecific steric repulsion is prevalent in all living cells and cannot be avoided. Later, ‘macromolecular confinement’ was distinguished from crowding to describe the situation that occurs when a molecule is within an enclosure or pore such as between the actin filaments in the cytoplasm or the central cage of a molecular chaperone (1, 2, 4, 5). The level of macromolecular crowding can vary, depending on the intracellular location, whether the cell experiences osmotic stress, and the specific cell type (1, 6). Thus, the dynamic nature of crowding makes it particularly challenging to study, both quantitatively and non-invasively.

1.3 Role of macromolecular crowding (in vivo)

Although the concept of crowding has long been established, its effects and significance remains unclear. Classical biological experiments ensure that parameters such as pH, ionic strength, and redox potential mimic those of the intracellular environment. However, these dilute solutions (1–10 g/L) do not account for the effects of macromolecular crowding (200–300 g/L), which can lead to experiments in buffers deviating greatly from the relevant physiological environments (1, 7, 8). This omission has profound consequences because a macromolecule is affected both kinetically and thermodynamically by crowding (9). Many experimental and theoretical studies have concluded that crowding affects reaction rates (8, 10, 11), protein folding and association (12-17), and biochemical signaling (18, 19), as well as many other essential processes. For example, increased aggregation of amyloid fibrils due to crowding may affect the causes of Parkinson's and Alzheimer's disease (20-25). More recent studies have focused on intrinsically disordered protein (IDPs) stability in various cellular compartments where the levels of crowding agents are known to fluctuate (26, 27). It was found that the stability of the IDPs was largely dependent on the soft interactions between the protein and the crowding agent indicating the dynamic nature of crowding (26). The effects on classical biological experiments and the consequences to health-related studies make understanding and quantifying macromolecular crowding of great importance.

1.4 Theory and experimental studies of cellular crowding

Studies investigating macromolecular crowding have been performed *in silico* (28-30), *in vitro* (25, 29-32), and *in vivo* (27, 31). Early experiments focused on excluded volume that describes crowding as simple steric repulsion (1, 8, 9, 32). The excluded volume effect is commonly mimicked *in vitro* with inert polymers such as Ficoll (33, 34) and dextran (17, 35). Recently, it became apparent that crowding is a combination of hard interactions (excluded volume) (36) and soft (or weak) chemical interactions (e.g., electrostatic, hydrogen bonding, hydrophobic) (26, 37-39). In some instances, the attractive and repulsive forces due to soft interactions can overcome the stabilizing effect

of excluded volume (26, 40). To mimic both hard and soft interactions, crowding agents such as bovine serum albumin, ovalbumin, and λ-globulins have been used *in vitro* (26, 37, 39, 41, 42). Monte Carlo and molecular dynamic simulations have also been used in an attempt to predict the effects of crowding on protein diffusion and folding (28-30). Common shortfalls of these simulations include a lack of experimental verification and inability to mimic the heterogeneous nature of crowding. Recent in-cell NMR spectroscopy measurements of crowding have focused on protein-protein interactions. However, these studies only provide accurate crowding effects for a particular protein and crowding agent (27, 31). Thus, an experimental technique is needed that is both quantitative and non-invasive with molecular sensitivity. This technique must also be amenable to the heterogeneous nature and the length- and time-scale dependence associated with crowding.

1.5 The need for crowding sensors: a family of FRET-based crowding sensors

Förster resonance energy transfer (FRET) is a widely used and powerful tool with the capacity to measure binding interactions (43, 44), conformational changes (45), and molecular distances (46). FRET involves non-radiative energy transfer from an excited donor molecule to a neighboring acceptor molecule in the ground state that form a FRET pair (47). The extent of energy transfer depends on the spectral overlap between the donor's emission and the acceptor's absorption, the distance between the donor and acceptor, and the relative orientation of the donor's emission dipole and the acceptor's absorption dipole (48, 49). The sensitive distance-dependence of FRET has led to its use as a molecular ruler to study intermolecular interactions in both solution and living cells with nanometer resolution (50).

Recently, Boersma *et al.* (51, 52) developed a series of FRET probes based on green fluorescent protein (GFP) mutants that can be expressed to measure the extent of crowding within a living cell. All of these probes consist of a hetero-FRET pair of mCerulean3 (53) (cyan fluorescent protein) and mCitrine (yellow fluorescent protein) connected by a linker that varies in length and rigidity. These linkers contain flexible

regions represented by (GSG_x) and rigid helices represented by ($EAAAK_x$). In this Thesis, we investigate five of these FRET probes (Fig. 1.1, Table 1.1). In a crowded environment, these FRET probes are hypothesized to become confined and more compact, thereby leading to enhanced energy transfer. Consequently, the level of crowding can be quantified based on the energy transfer efficiency of the probes.

Table1.1: Detailed features of the probes. The MW was estimated from the amino acid sequence.

Acronym	Linker Sequence	Amino acids in linker	EAAAK / GSG	MW (Da)
GE	$(GSG)_6A(EAAAK)_6A(GSG)_6A(EAAAK)_6A(GSG)_6$	114	0.67	63,957
E6G2	$A(EAAAK)_6A(GSG)_6A(EAAAK)_6A$	66	6	60,796
E6	$(GSG)_6A(EAAAK)_6A(GSG)_6$	66	0.5	59,842
G18	$(GSG)_{18}$	54	0	58,084
G12	$(GSG)_{12}$	36	0	56,876

Using steady-state spectroscopy, Boersma *et al.* (51, 52) demonstrated the sensitivity of the probes in crowded environments based on the intensity ratio of mCerulean3/mCitrine. This qualitative FRET ratio suffers from complications due to the spectral overlap between the donor's emission and the acceptor's absorption. Steady-state spectroscopy is additionally unable to resolve an increase in FRET efficiency versus an increase in the FRET population (54, 55).

Fluorescence lifetime measurements are also a common technique to assess FRET efficiency (50, 56, 57). However, lifetime measurements suffer from errors in the local refractive index of the environment which is very complex and dynamic in living cells (58). Additionally, lifetime measurements assume monoexponential decays for fluorophores to calculate energy transfer efficiency in the FRET pair (59, 60). Both steady-state spectroscopy and fluorescence lifetime are incapable of accounting for conformational dynamics of the different FRET probes in homogenous and heterogeneous environments, which is essential for their characterization before proceeding with *in vivo* studies. To overcome these challenges, a complementary

approach that is both quantitative and non-invasive is needed to assess FRET efficiency with sensitivity to conformational changes and fluorescence depolarization. Additionally, a technique to describe the conformational dynamics of the probes that is amenable to the multidimensional nature of crowding is essential.

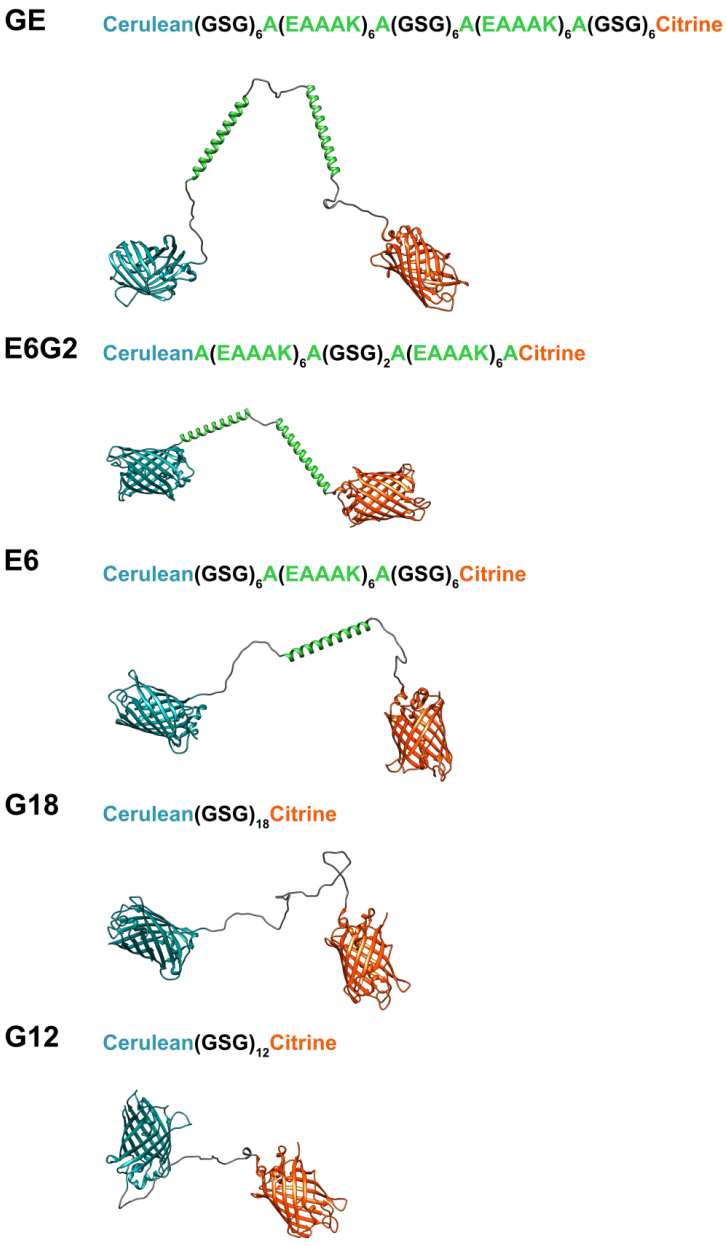

Figure 1.1: Representative structures of the five FRET probes characterized in this Thesis. All probes consist of a mCerulean3 donor and mCitrine acceptor connected by a linker that varies in length and rigidity.

1.6 Quantitative, noninvasive methods for investigating in vitro macromolecular crowing

The drawbacks of steady-state spectroscopy and lifetime measurements that include a lack of sensitivity and inability to investigate conformational dynamics reveals the need for an additional technique. To address the inherent heterogeneous and dynamic nature of intracellular crowding and its effect on the diffusion of the probes, we use time-resolved anisotropy. Time-resolved anisotropy allows us to measure the conformational changes and rotational dynamics that take place on the ps–ns timescale. Thus, we can determine the hydrodynamic volume of the different probes based on their overall rotational times. This approach allows us to describe the conformational variability of the FRET probes based on their linker length and flexibility. In the context of crowding, we hypothesize that excluded volume will induce a compaction of the probe resulting in an increase in FRET efficiency. Using time-resolved anisotropy, depolarization due to FRET can be distinguished from the slower overall rotation of the probe, due to the relatively fast time scale of FRET. The presence of FRET has largely been described qualitatively using time-resolved anisotropy decays. More recently, Warren *et al.* (61) derived a model to quantify homo-FRET aggregation using time-resolved anisotropy. However, this model does not provide accurate measurements of FRET efficiency when applied to hetero-FRET. Therefore, to quantify crowding using time-resolved anisotropy, a model for hetero-FRET must be established.

In Chapter 3, I describe our efforts to model hetero-FRET using time-resolved anisotropy to calculate the varying FRET efficiencies of the probes. This model successfully agrees with traditional FRET efficiencies calculated from fluorescence lifetime. In Chapter 4, I describe our characterization of the probes in homogenous environments including buffer and glycerol-enriched buffer as a control for crowding studies. Finally, in Chapter 5, the effects of excluded volume on FRET efficiency of the five probes are investigated.

Chapter 2
Materials and methods

2.1 Overview

This Chapter describes the purification of the FRET probes and the theory of time-resolved anisotropy. Here, anisotropy measurements are used to assess the excited–state rotational dynamics of the FRET probes on the nanosecond timescale. Anisotropy can also be used to determine the energy transfer efficiency of the various probes. The sample preparation, experimental design, and all relevant equations are also described.

2.2 Materials and methods of FRET probe purification

The design of the genetically encoded FRET probe, GE, has been described in detail elsewhere (51). Briefly, in this probe mCerulean3 (53) (cyan fluorescent protein; 27.5 kDa) and mCitrine (yellow fluorescent protein; 27.0 kDa) serve as the donor and acceptor of the FRET pair, respectively. As shown in Figure 1.1, mCerulean3 at the N terminus is connected by a flexible linker to mCitrine at the C terminus. It is important to note that both fluorescent proteins contain an A206K mutation to inhibit self-association (62). A series of five newly developed probes with varying linker lengths and flexibility were purified and examined in this Thesis to assess their effectiveness at measuring crowding (Fig. 1) (52).

Plasmids of the five constructs in pRSET host vectors were obtained from Arnold J. Boersma (University of Groningen, the Netherlands), transformed into the *E. coli* strain BL21(DE)pLysS (Invitrogen), and plated on LB-agar plates containing 100 μg/mL ampicillin. Successfully transformed colonies were selected and inoculated into 2 mL of LB (100 μg/mL ampicillin) and shaken overnight at 37°C. Half of the overnight culture was used to conduct an alkaline lysis mini prep and an analytical restriction digest to confirm the correct plasmid DNA. Following confirmation, a glycerol stock of the transformed *E. coli* was prepared and stored at –80°C for all future cultures.

The following procedure was used to purify the five FRET probes. A scrape of the frozen glycerol stock was inoculated into 2.5 mL of TB medium (1.2% bactotryptone, 2.4% yeast extract, 0.4% glycerol, 1.4% (w/v) potassium phosphate, pH 7.5) with 1 mg/mL ampicillin and shaken overnight at 37°C. One mL of overnight culture was placed into two baffled flasks containing 25 mL of TB medium each and grown at 30°C to an OD of 0.6, as measured by a NanoDrop™ 2000 spectrophotometer. The cells were induced overnight with 0.1 mM isopropyl-β-D-thiogalactoside (IPTG) at 25°C. The cells were centrifuged at 5,000 rpm (Beckman J25.5, 3000 × g) for five min at 4°C and resuspended with 8 mL of lysis buffer (10 mM sodium phosphate, 100 mM sodium chloride, 0.1 mM phenylmethylsulfonyl fluoride [PMSF], 1 mg/mL lysozyme, pH 7.4) and incubated on ice for 30 min. The lysate was sonicated on ice and drawn up with an 18.5 gauge needle five times to shear DNA and other debris and incubated on ice for one hr. The lysate was clarified at 5,000 rpm (Beckman J25.5, 3000 × g) for 15 min at 4°C and imidazole was added to the supernatant to a final concentration of 10 mM. A column of ProBond™ nickel-chelating resin (Life Technologies) was equilibrated four times with binding buffer (10 mM sodium phosphate, 100 mM sodium chloride, 10 mM imidazole, pH 7.4). The lysate was then loaded onto the equilibrated column and rocked for one hour at room temperature. The column was washed four times with wash buffer (50 mM sodium phosphate, 300 mM sodium chloride, 20 mM imidazole, pH 8.0). The protein was eluted with 8 mL of elution buffer (50 mM sodium phosphate, 300 mM sodium chloride, 250 mM imidazole, pH 8.0). The peak fraction was dialyzed against phosphate-buffered saline (1× PBS; pH 7.4) at 4°C using a Slide-A-Lyzer (ThermoScientific, MWCO 3.5 kDa). The purified protein was stored at 4°C and used within two weeks of preparation. The purified protein was analyzed using 12% SDS-PAGE gel and visualized using Coomassie staining (Fig. A1.1). The absorption and emission spectra were determined using a Beckman Coulter DU800 spectrophotometer and a Horiba Jobin Yvon Fluorolog, respectively. In Figure 2.1, the absorption band at 280 nm (ε = 54,000 M^{-1} cm^{-1}) was used to calculate the concentration of the purified FRET probe.

To disrupt FRET between the donor (mCerulean3) and the acceptor (mCitrine), the flexible linker region (GSG_x) of the FRET probe was digested using the serine protease, proteinase K. This cleavage serves as a control for energy transfer between mCerulean3 and mCitrine. For this cleavage, 0.56 ng of proteinase K (Sigma-Aldrich) was added per µmol of the purified probe. After 1 minute incubation at 25°C, 20 µmol of PMSF per mg of proteinase K was added to terminate the cleavage reaction by this serine protease. SDS-PAGE analysis was used to determine the extent of the proteolytic cleavage as compared with the control of intact protein for which no proteinase K was added (Fig. A1.2).

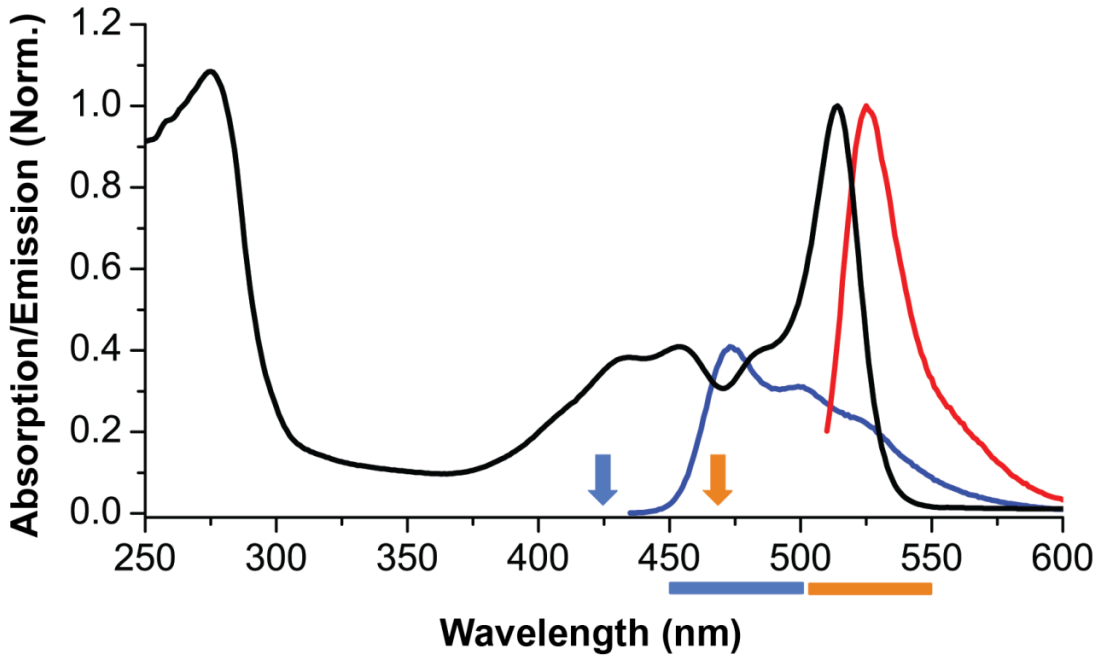

Figure 2.1: Absorption spectrum of GE probe (black curve) as well as the emission spectra of both the donor (excited at 425 nm) and acceptor (excited at 465 nm). The arrows indicate the excitation wavelengths used in the anisotropy measurements in this Thesis. The horizontal lines indicate the width of the bandwidth emissions filters for the donor (blue curve) and acceptor (red curve) fluorescent detections. The absorption and emission bands are normalized for both the donor and acceptor.

2.3 Materials and methods of biomimetic crowding

PBS (Invitrogen; pH 7.4) was used for all sample preparation in this Thesis. To mimic heterogeneous crowding in cellular environments, Ficoll-70 (Santa Cruz Biotechnology) was used at concentrations up to 300 g/L. Ficoll-70 is a nonionic synthetic sucrose polymer with an approximate molecular weight of 70 kDa. To control for homogenous viscosity, glycerol-enriched PBS was used under the same experimental conditions. Concentrations up to 760 g/L were prepared with concentrated glycerol (≥99.5%; Fisher Scientific) to account for a range of viscosities found *in vivo* and the equivalent viscosity introduced by Ficoll-70 (Fig. A2.1, Table A2.1).

2.4 Materials and methods of time-resolved anisotropy

2.4.1 Theory of time-resolved anisotropy

Time-resolved anisotropy is a means of measuring the rotation of a fluorophore. Upon excitation with a polarized laser pulse, the fluorophores whose absorption dipoles align with the electric field of the laser will become preferentially excited. As a result of this photoselective excitation, the emission of the fluorophore will also be partially polarized at time zero. The probability of photoselective excitation (p) at this time can be described by the angle (θ) between the excitation polarization and the absorption dipole such that:

$$p_{excitation} \propto \cos^{x} \theta \tag{2.1}$$

Following such excitation with polarized light ($t > 0$), the fluorescence emission becomes depolarized due to thermal energy-induced rotational motion (Fig. 2.2). The dipole orientation can be monitored over time using polarization, and the subsequent analysis can provide a wealth of valuable information about the molecular system (63). The orientation of the emitting dipole can become depolarized due to the rotational motion of the fluorophore, the conformational changes of the fluorophore while in the excited state, ultrafast non-radiative processes, and FRET to a fluorophore with a different dipole orientation.

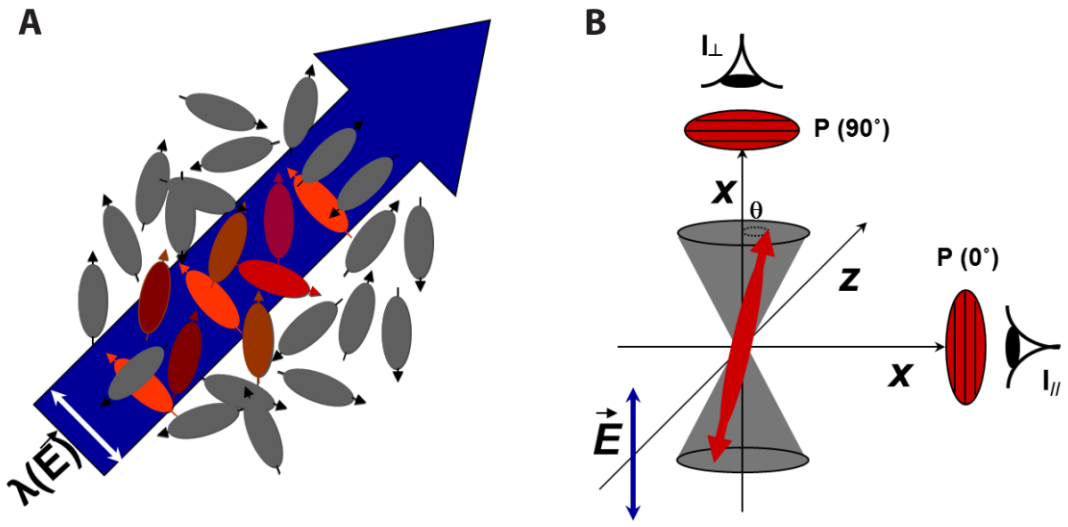

Figure 2.2 Photoselection and absorption dipole orientation. A) photoselection of fluorophores whose dipoles align with incoming polarized light. B) Radial probability of photoselection and detection of polarization emission.

Depolarization due to FRET occurs when a photoselected donor fluorophore transfers its energy in a non-radiative mechanism to an acceptor fluorophore. The rapid energy transfer from donor to acceptor result in a fast apparent depolarization rate (k_{ET}) due to the acceptor's dipole being more randomly oriented (Figure 2.3). Accordingly, the extent of FRET between the probes such as those described in this Thesis can be characterized by exciting the donor and detecting the fluorescence emission of the acceptor.

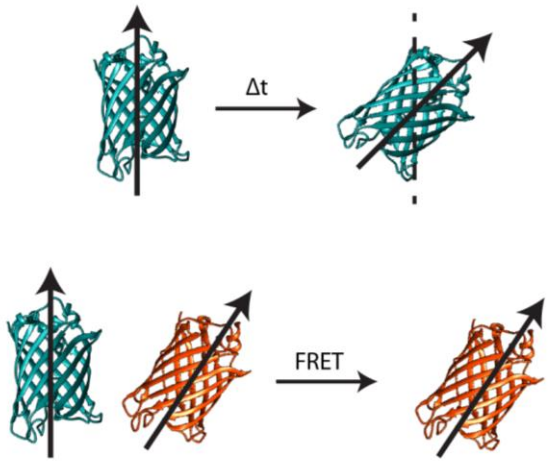

Figure 2.3 Schematic of depolarization due to rotation and FRET.

The corresponding energy transfer efficiency (*E*) can be calculated using both k_{ET} and the fluorescence lifetime of the donor (τ_D) such that (48):

$$E = \frac{k_{ET}}{\tau_D^{-1} + k_{ET}} \tag{2.2}$$

In these experiments, τ_D was determined after proteolytic cleavage of the linker in the FRET probe to obtain the fluorescence lifetime of the donor alone. The fluorescence lifetime describes the average amount of time a fluorophore remains in the excited state (64). The corresponding distance between the donor and acceptor (R_{DA}) in the intact FRET probe in crowded environments can subsequently be determined based on the E and the Förster distance (R_0) such that:

$$R_{DA} = R_0 \left(\frac{1}{E} - 1 \right)^{1/6} \tag{2.3}$$

R_0 depends on the spectral overlap between the donor's emission and acceptor's absorption spectra (Fig. 2.1) as well as their orientation parameter (κ^2) which was assumed to be 2/3. This κ^2 value assumes the fluorophores are randomly oriented in solution and does not result in major errors in the Förster distance calculations (50, 65). For our donor (mCerulean3) and acceptor (mCitrine), the calculated R_0 is 5.26 nm in phosphate-buffered saline (Table A3.1).

2.4.2 Experimental setup and calibration

The rotational dynamics of the FRET probes were characterized using the time-correlated single-photon counting (TCSPC) technique. The experimental setup is shown in Figure 2.3. Femtosecond infrared laser pulses (850 or 930 nm) were generated using a titanium-sapphire solid-state laser system (Mira 900-F, Coherent). A droplet of sample was positioned on a coverslip on a 1.2 NA 60× water immersion microscope objective (Olympus UPlanApo/IR). One-photon laser pulses (425 and 465 nm) were generated to excite the sample at a 4.2 MHz repetition rate. A 475 filter with a FWHM of 50 was used for detecting the donor. For detection of the acceptor a 531 filter with a FWHM of 40 was

used. From here on, the convention maximum/FWHM will be used to identify the bandpass filters (e.g. 531/40). The filtered wavelength-dependent fluorescence was polarization-analyzed, detected, amplified, and routed to a synchronized SPC-830 module (Becker & Hickl) for data acquisition. A polarizing beam splitter was used to isolate the parallel and perpendicular fluorescence polarizations (with respect to the laser polarization), which were detected simultaneously using two microchannel plate (MCP) photomultiplier tubes (R3809U, Hamamatsu). The laser was calibrated using the anisotropy of rhodamine 110 (Rh110; rotational time of ~140 ps) and coumarin (rotational time of ~98 ps) to assess the wavelength dependence of the G-factor. A standard was run at the start and end of each experiment to validate the stability of the laser during data collected (66).

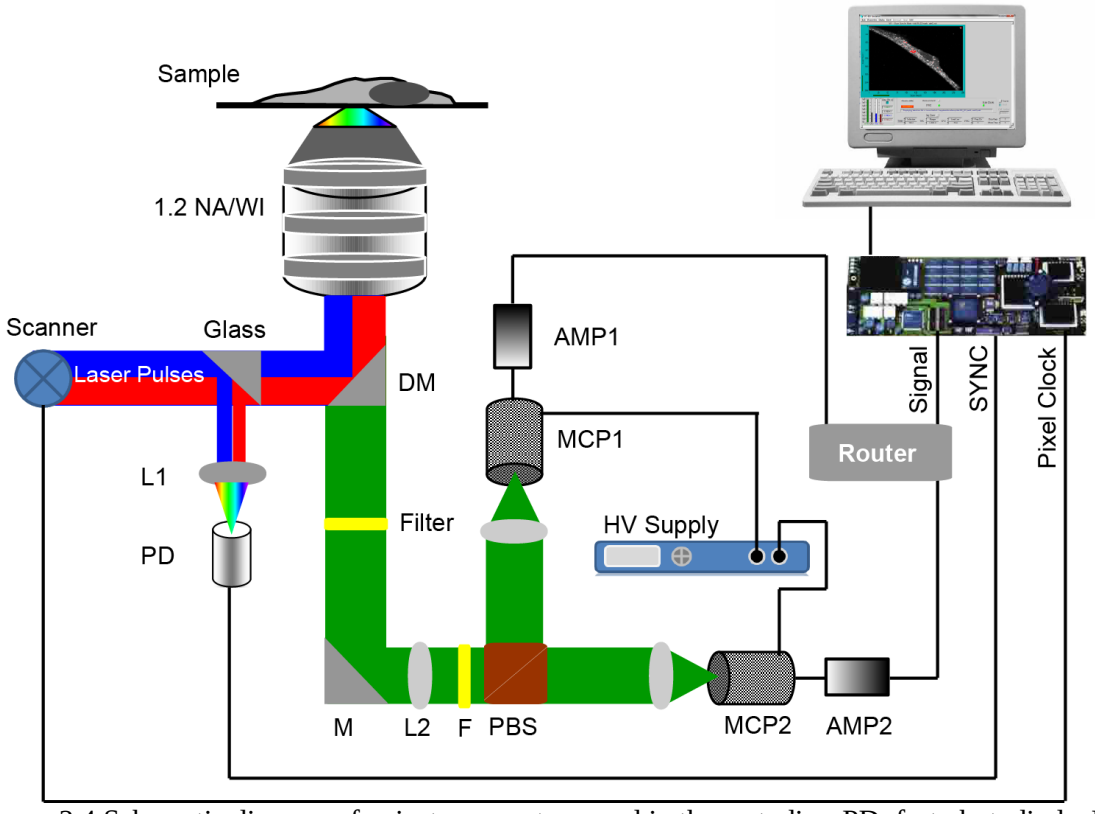

Figure 2.4 Schematic diagram of anisotropy system used in these studies. PD: fast photodiode, L: lens, DM: dichroic mirror, F: filter, PBS: polarizing beam splitter, MCP: microchannel plate, AMP: amplifier.

2.4.3 Data analysis

The time-resolved anisotropy, $r(t)$, was calculated using the parallel ($I_{\parallel}(t)$) and perpendicular ($I_{\perp}(t)$) fluorescence decays such that (48):

$$r(t) = \frac{I_{\parallel}(t) - GI_{\perp}(t)}{I_{\parallel}(t) + 2I_{\perp}G(t)} = \sum_i \beta_i e^{-t/\varphi_i} \tag{2.4}$$

The sum of the fractional amplitudes of a multi-exponential decay (β_i) is equal to the initial anisotropy (r_0), which describes, in theory, the anisotropy observed in the absence of any depolarizing factors such as a fluorophore fixed in a matrix or gel (67). The initial anisotropy cannot exceed 0.4, which describes a molecule where the parallel and perpendicular decays are collinear (i.e., frozen in space) (48). Hence, the lower the initial anisotropy (r_0), the greater the extent of depolarization due to different mechanisms that may include FRET. The φ in equation 2.4 describes the rotational diffusion time of molecule of interest. The geometrical factor (G-factor) was determined using the tail-matching approach that eliminates any polarization-biased detection. The factor of 2 in the denominator of equation 2.4 accounts for the depolarization caused by the high numerical aperture of the microscope objective. Because such depolarization does not affect the anisotropy decay time constant, we use the traditional anisotropy model (Eq. 2.4), particularly for the under-filled microscope objective (68). The quality of the fit was judged using both the χ^2 and the residuals. The anisotropy decays were analyzed using OriginPro software.

When the polarizer in the emission path is oriented at the so called magic angle (MA), 54.7°, with respect to the vertical intensity, the fluorescence lifetime can be determined based on the total fluorescence intensity represented by the denominator in equation 2.4 such that (67, 69):

$$I_{MA} = I_{\parallel} + 2GI_{\perp} = \sum_i \alpha_i e^{-t/\tau_i} \tag{2.5}$$

where α_i is the amplitude of a multi-exponential lifetime decay. Equation 2.5 will later allow us to determine the fluorescence lifetimes needed for calculations of FRET efficiency.

For steady-state anisotropy (r_{ss}), the time-resolved parallel and perpendicular polarization fluorescence were integrated such that (48):

$$r_{ss} = \frac{\int I_{\parallel}(t)\,dt - G\int I_{\perp}(t)\,dt}{\int I_{\parallel}(t)\,dt + 2G\int I_{\perp}(t)\,dt} \propto \cos\left(\theta\right) \tag{2.6}$$

where θ is the angle between the absorbing and emitting molecular dipole. The steady-state anisotropy and initial anisotropy in time-resolved measurements are related by the Perrin-Weber equation (48):

$$\frac{1}{r_{ss}} = \frac{1}{r_0} + \frac{\tau}{\varphi} = \frac{1}{r_0} + \frac{\tau k_B}{V}\frac{T}{\eta} \tag{2.7}$$

where (k_B) is the Boltzmann's constant and T is temperature. The Perrin-Weber equation can be used to calculate the apparent volume of a protein as a function of the bulk viscosity (η). Assuming the Stokes-Einstein model for a spherical molecule, the hydrodynamic volume (V) of the probe can also be calculated based on the bulk viscosity of the surrounding environment and the probe's corresponding rotational diffusion rate (D_R) such that (70):

$$D_R = \frac{k_B T}{6\eta V} \tag{2.8}$$

where the hydrodynamic volume assumes the diffusing moiety is a sphere. If the FRET probe follows the Stokes-Einstein model of diffusion, the diffusion coefficient ratio (D_0 / D_c) of the probe should be linearly proportional to the bulk viscosity ratio (η_c / η_0) such that:

$$\frac{D_0}{D_c} = \frac{\eta_c}{\eta_0} \tag{2.9}$$

where the subscript "0" indicates the diffusion coefficient of the FRET probe in pure PBS buffer and the subscript "c" refers to glycerol- or Ficoll-enriched buffers. Using the slow

rotational time of the FRET probes in the measured anisotropy decays we are able to calculate the rotational diffusion rate (D_R) according to:

$$\varphi = \frac{\eta V}{k_B T} = \frac{1}{6D_R} \tag{2.10}$$

The rotational time of a molecule is also approximately related to its molecular weight (MW) by:

$$\varphi = \frac{\eta MW}{k_B T}(\nu_0 + h) \tag{2.11}$$

where $(\nu_0 + h)$ accounts for the partial specific volume of the protein based on the level of hydration because proteins do not exist as anhydrous spheres. For most proteins this value is approximately 0.96 ml/g.

Using these polarization based methods, we hypothesize that by varying the excitation and detection wavelengths we will be able to distinguish between depolarization due to rotational motion and energy transfer (FRET). When exciting the donor and detecting the donor, we hypothesize that the anisotropy decay will represent depolarization strictly due to overall rotation. However, when exciting the donor and detecting the acceptor, the anisotropy will decay as a biexponential with a slow component describing the rotation and a fast component representative of energy transfer. In Chapter 3, we propose a model of hetero-FRET using time-resolving anisotropy to quantify the amount of energy transfer based on the biexponential behavior. The wavelength-dependent anisotropy decays of the five FRET probes will be characterized in homogenous and heterogeneous environments in Chapter 4 and 5, respectively.

Chapter 3
Modeling fluorescence depolarization due to FRET using time-resolved anisotropy

3.1 Background

Traditionally, time-resolved anisotropy measurements provide information about the conformational dynamics and sizes of molecules based on rotational mobility. More recently, anisotropy measurements have been expanded to monitor the presence of FRET (71-74). However, these measurements have largely been qualitative and rely on relative trends in the anisotropy decays of homo-FRET. To quantify the level of crowding using time-resolved anisotropy, we derived a model to determine the energy transfer efficiency of the FRET probes in various environments.

3.2 Results and discussion

3.2.1 Kinetic model of anisotropy in the presence of FRET-based depolarization

Using time-resolved anisotropy, the rotational mobility of a fluorophore underlies the depolarization of the fluorescence emission following the polarized excitation pulse of a photoselected population of molecules. In time-resolved anisotropy, the parallel and perpendicular polarizations of the depolarized fluorescence are analyzed. According to the Stokes-Einstein model, the rotational decay time of a spherical molecule is inversely proportional to the hydrodynamic volume of the fluorophore in a given environment.

We hypothesize that the rotational dynamics of a hetero-FRET probe with a flexibly linked donor-acceptor pair will be wavelength dependent due to the two competing depolarization mechanisms of rotational motion and energy transfer. The excitation and detection of the donor alone in a hetero-FRET probe would lead to a single exponential anisotropy decay with a time constant dictated solely by the depolarization due to the tumbling motion of the donor alone such that:

$$r_{DD}(t) = r_0 e^{-t/\varphi} \tag{3.1}$$

where r_0 is the initial anisotropy and φ is the rotational time of the donor.

This scenario is likely to be the case even in the presence of two populations of the FRET probe: one undergoing energy transfer and the other that does not undergo FRET based on the instantaneous relative orientations of the dipole moments of the donor and acceptor as well as the intermolecular distance between the donor and acceptor.

When the donor is excited and the acceptor is detected, however, the time-resolved anisotropy of a hetero-FRET probe will decay as a biexponential. Let's assume a population of the FRET probe is excited by a polarized laser pulse at time zero. Immediately after this pulsed photoselection, we assume that a fraction of the population (f_D) will undergo depolarization due to rotational mobility (i.e., at rate of φ^{-1}). The remaining fraction of the population (f_A) will undergo depolarization due to both rotational mobility and energy transfer rate (i.e., $k_{ET} + \varphi^{-1}$). FRET will depolarize the emission due to the more randomly oriented dipole of the acceptor. Under these assumptions, we predict a biexponential anisotropy decay for these two such populations where:

$$r_{DA}(t) = f_D r_{D0} e^{-(\varphi^{-1})t} + f_A r_{A0} e^{-(\varphi^{-1} + k_{ET}^{*})t} \tag{3.2}$$

The fraction (f_D) of the population undergoing rotational depolarization can be estimated by the corresponding signal contribution such that:

$$f_D = \frac{\alpha_1 e^{-(k_{fl}^{D})t} + \alpha_2 e^{-(k_{fl}^{D} + k_{ET}^{*})t}}{\alpha_1 e^{-(k_{fl}^{D})t} + \alpha_2 e^{-(k_{fl}^{D} + k_{ET}^{*})t} + \alpha_3 e^{-(k_{fl}^{A})t}} \approx \frac{\alpha_1 \tau_{fl}^{D} + \alpha_2 \left(k_{fl}^{D} + k_{ET}^{*}\right)^{-1}}{\alpha_1 \tau_{fl}^{D} + \alpha_2 \left(k_{fl}^{D} + k_{ET}^{*}\right)^{-1} + \alpha_3 \tau_{fl}^{A}} \tag{3.3}$$

The fluorescence signal contribution of the remaining fraction (f_A) of the population undergoing both rotation and energy transfer is given by:

$$f_A = \frac{\alpha_3 e^{-(k_{fl}^{A})t}}{\alpha_1 e^{-(k_{fl}^{D})t} + \alpha_2 e^{-(k_{fl}^{D} + k_{ET}^{*})t} + \alpha_3 e^{-(k_{fl}^{A})t}} \approx \frac{\alpha_3 \tau_{fl}^{A}}{\alpha_1 \tau_{fl}^{D} + \alpha_2 \left(k_{fl}^{D} + k_{ET}^{*}\right)^{-1} + \alpha_3 \tau_{fl}^{A}} \tag{3.4}$$

As a result, the time-resolved anisotropy of a hetero-FRET probe, in which we excite the donor and detect the acceptor, can be used to determine the energy transfer rate (k_{ET}^{*}).

The k_{ET}^{*} measured from anisotropy only represents the fluorophores that undergo FRET, instead of the entire population of excited fluorophores. Thus, the amplitude fractions of the populations must be accounted for to calculate the proper energy transfer rate, k_{ET}, such that:

$$k_{ET} = k_{ET}^{*}\left(\frac{f_A r_{A0}}{f_D r_{D0} + f_A r_{A0}}\right) \tag{3.5}$$

In addition, the rotational time constant of both the donor and acceptor of the FRET probe can also be estimated. These rotational times can be determined using careful experimental design based on the excitation and detection wavelengths combination that allow us to only monitor the donor or acceptor.

3.2.2 Simulation and theoretical prediction

The above mentioned developed model allows us to predict the time-resolved anisotropy profile of a FRET probe as a function of the energy transfer rate (k_{ET}) and excitation/detection wavelength. Using equation 3.2, we simulated the time-resolved anisotropy of the donor in the FRET pair, when excited at 425 nm and 475 nm. In the absence of energy transfer ($k_{ET} = 0$), the depolarization of the FRET probe is caused only due to its rotational motion. Assuming a rotational time of 20 ns for a probe, which is consistent with the probe sizes used in this project, the anisotropy associated with the donor's emission decays as a single exponential (Figure 3.1, green curve). As a result, an observed single exponential decay for the anisotropy of a FRET probe when the donor is being exciting and detected would indicate a fluorescence depolarization due to rotational motion alone with a rotational time that is consistent with the hydrodynamic volume of the FRET probe. In addition, the population of the excited/detected FRET probe under these conditions is unlikely to undergo depolarization due to FRET.

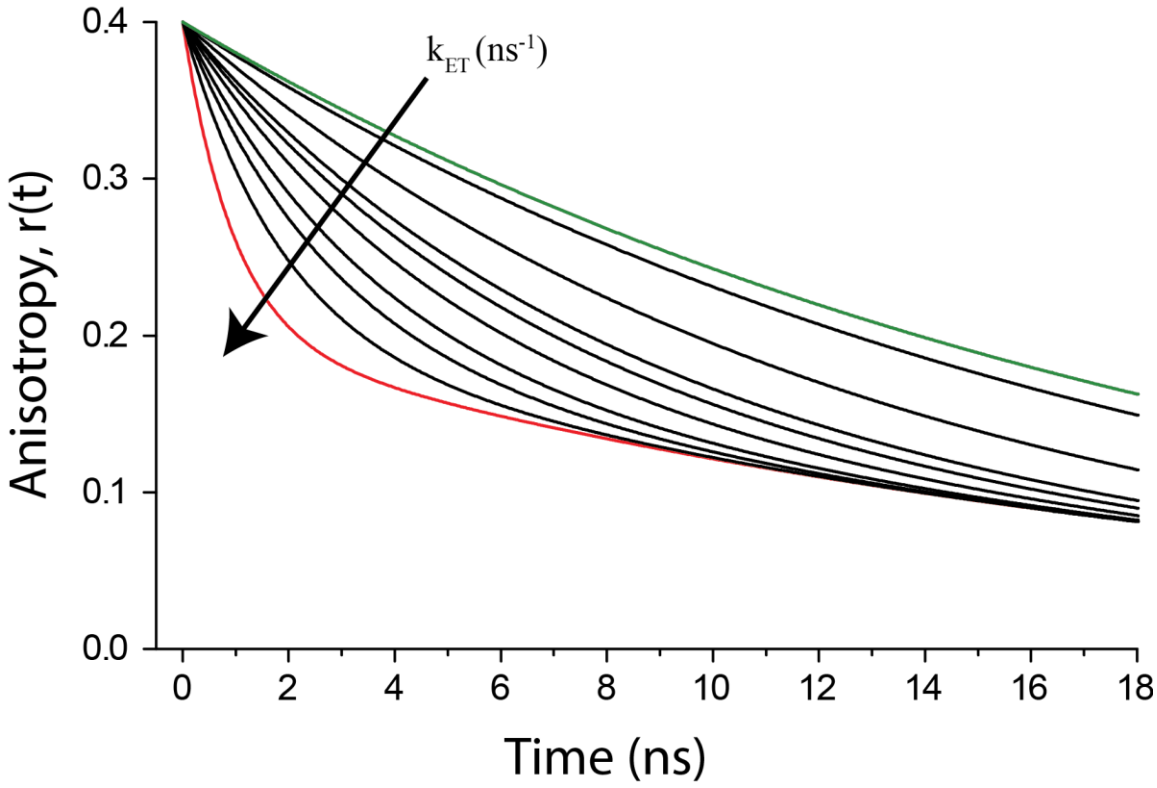

Figure 3.1: Simulated anisotropy decay based on equation 3.2. The green curve represents and an energy transfer rate of zero while the red curve represents and energy transfer rate of 1.

On the other hand, in the presence of a mixture of two populations of FRET probes, one that undergoes energy transfer and another that does not, the observed anisotropy decay is expected to be biexponential as shown in Figure 3.1. In this simulation, we also used a rotational time of 20 ns, but varied the energy transfer rate (k_{ET}) from 0.01 ns^{-1} to 1 ns^{-1} as a means to visualize how the time-resolved anisotropy profile may vary with the energy transfer efficiency. Keep in mind that this range of the energy transfer rate corresponds to energy transfer time of 100 ns and 1 ns as compared with the excited-state lifetime of 4.0 ns for the donor emission. In these anisotropy decay curves, the fast decay component is the sum of the rotational rate (φ^{-1}) and the energy transfer rate (k_{ET}). These curves account for two depolarization mechanisms (i.e., rotational motion and energy transfer) of the FRET probe emission, when excited at 425 nm and detected at 531 nm in our case. As the energy transfer rate increases, the corresponding decay time constant of the anisotropy decay component decreases as

shown in Figure 3.1. It is worth noting that the nature of the time-resolved anisotropy profile is expected to change with the relative population fractions (i.e., with and without FRET) in the assumed mixture of the FRET probes. For this simulation, it was assumed the population fractions each contributed 50%.

Taken together, this model and the associated simulation shown in Figure 3.1 will be tested using our wavelength-dependent measurements of the time-resolved anisotropy of the FRET probes as a function of both the linker length/flexibility and the surrounding environments. In addition, we predict that exciting the donor and detecting the emission of the acceptor in a hetero-FRET pair would allow us to calculate the energy transfer rate and therefore the energy transfer efficiency for each construct investigated in this Thesis. Importantly, the model developed here is likely to be used in a wide range of FRET probes that might go beyond our five constructs. The outcome in this case would depend on the experimental design and the donor-acceptor spectral overlap of those FRET probes.

Chapter 4
Rotational diffusion of FRET probes in homogenous environments

Disclosure: This chapter has been published, in part, in the following:

Currie, M.; Leopold, H.; Schwarz, J.; Boersma, A. J.; Sheets, E. D.; Heikal, A. A., Fluorescence dynamics of a FRET probe designed for crowding studies. *The Journal of Physical Chemistry B* **2017,** *121* (23), 5688-5698.

4.1 Background

Here we used time-resolved anisotropy to measure the rotational dynamics of the FRET probes on the ps–ns time scale. To assess how the probes are behaving in complex heterogeneous environments such as those present in macromolecular crowding, we must first have a good understanding of their behavior in a well-controlled homogenous environment. Thus, we investigated the wavelength dependence of the FRET probes in buffer at room temperature. By exciting and detecting the donor, we can investigate the flexibility of the linker based on the donor's ability to undergo rotational diffusion. We can also excite the donor and detect the acceptor to assess energy transfer because any fluorescence we detect under these conditions results from FRET because the acceptor is not being directly excited. Based on our time-resolved anisotropy measurements in phosphate-buffered saline, we can elucidate the size and conformational rigidity of the five FRET probes with varying linkers. These measurements also allow us to test the validity of our model in assessing energy transfer efficiency at various excitation and detection wavelength combinations.

As a control for homogenous viscosity, we also conducted time-resolved anisotropy in glycerol-enriched buffer at room temperature. Ficoll-70 (Chapter 5) introduces heterogeneous viscosity, which affects the rotational diffusion of the probes according to equation 2.8. Therefore a viscosity control is essential to distinguish between changes in FRET efficiency due to viscosity and those that can be attributed to excluded volume effects. A range of glycerol concentrations from (0–760 g/L) were used which corresponds to a viscosity range of 0.89–18.2 cP at room temperature (Table

A2.1). This concentration range was selected to account for the viscosity introduced by Ficoll-70. We also used equation 2.7 to describe how the polarized emission is affected by fast processes such as energy transfer.

4.2 Results and discussion

4.2.1 Wavelength dependence of rotational dynamics in PBS

To assess the wavelength dependence of the rotational dynamics of the FRET probes, we carried out time-resolved anisotropy as function of excitation and detection wavelength. With these measurements, we were able to determine how the linker length and its flexibility affect the energy transfer efficiency of the five probes studied in this Thesis. Representative anisotropy decays for the intact and cleaved E6 probe in buffer (PBS, pH 7.4) at room temperature are shown in Figure 4.1. Under 425 nm illumination (donor excitation), the polarization-analyzed fluorescence (475/50 nm) of the donor (mCerulean3) was detected, and the corresponding anisotropy of the intact E6 probe decays as a single exponential with a rotational time of (17.8 ± 0.2) ns (Figure 4.1A and Table 4.1). If the decay is fit to a biexponential, the χ^2 only increases by 3%, resulting in a second component that only contributes 6% to the total decay. Hence, a single exponential was chosen to ensure the decay was not being over-parameterized. The error reported throughout this Thesis represents the standard error of the fitting parameters of a single trial. Under the same conditions, the anisotropy decay of cleaved E6 also decays as a single exponential with a faster rotational time of (13.3 ± 0.08) ns, which is greater than half of the overall rotational time of the intact E6. The observed rotational time of the intact E6 donor is too fast to be assigned to the overall rotation of the intact probe (60 kDa) which is predicted to be 20.6 ns based on the Stokes-Einstein model (Eq. 2.11). We attribute this observation to the local motion of E6 because the donor alone rotates around the linker as compared with the entire molecule rotating as a single unit. In addition, our observed single-exponential anisotropy decay indicates that depolarization of the donor emission is primarily due to its rotational mobility, which agrees with our model that predicts a single exponential decay when k_{ET} is equal to zero.

Under 425 nm excitation of the donor and detection of the acceptor (531/40 nm) of the E6 probe, the anisotropy decays as a biexponential with an overall rotational time of (18.0 ± 0.4) ns (β_2 = 0.184 ± 0.002) along with a fast time component of (1.47 ± 0.13) ns (β_1 =0.074 ± 0.003). This fast component is too fast to be assigned to the overall rotation of an acceptor of that size (27 kDa) which is predicted to be 9.3 ns based on the Stokes-Einstein model (Eq. 2.11). Additionally, the fast component is absent from the cleaved E6 probe (Fig. 4.1B). We attribute the fast component to FRET which would cause a rapid depolarization of the anisotropy decay due to energy transfer between the donor and acceptor (Figure 2.3). An emission overlap between the donor emission and acceptor excitation of the probe can be seen in Figure 2.1, which demonstrates the potential for energy transfer to occur. Based on our model of FRET efficiency using anisotropy outlined in section 3.2, we used our fitting parameters to estimate an energy transfer efficiency of (20.5 ± 0.8) %. This efficiency was weighted by the population fraction of E6 undergoing energy transfer in buffer to determine the efficiency of the entire population versus just the population undergoing FRET (Eq. 3.5). These results are in general agreement with our energy transfer efficiencies that were determined using fluorescence lifetime (Table A3.2). Such agreement provides support for our time-resolved anisotropy approach for FRET studies of hetero-FRET probes.

Under 465 nm excitation and 531/40 nm detection, both the donor and acceptor in E6 can be excited and detected, albeit with different efficiencies (Fig. 2.1). For this reason, the anisotropy also decays as a biexponential (Table 4.1) with a smaller amplitude fraction undergoing a fast depolarization mechanism. The rationale for the observed fast anisotropy decay, with a smaller amplitude fraction, is that direct excitation/detection of the FRET pair undermines the energy transfer contributions at a rate of k_{ET} .

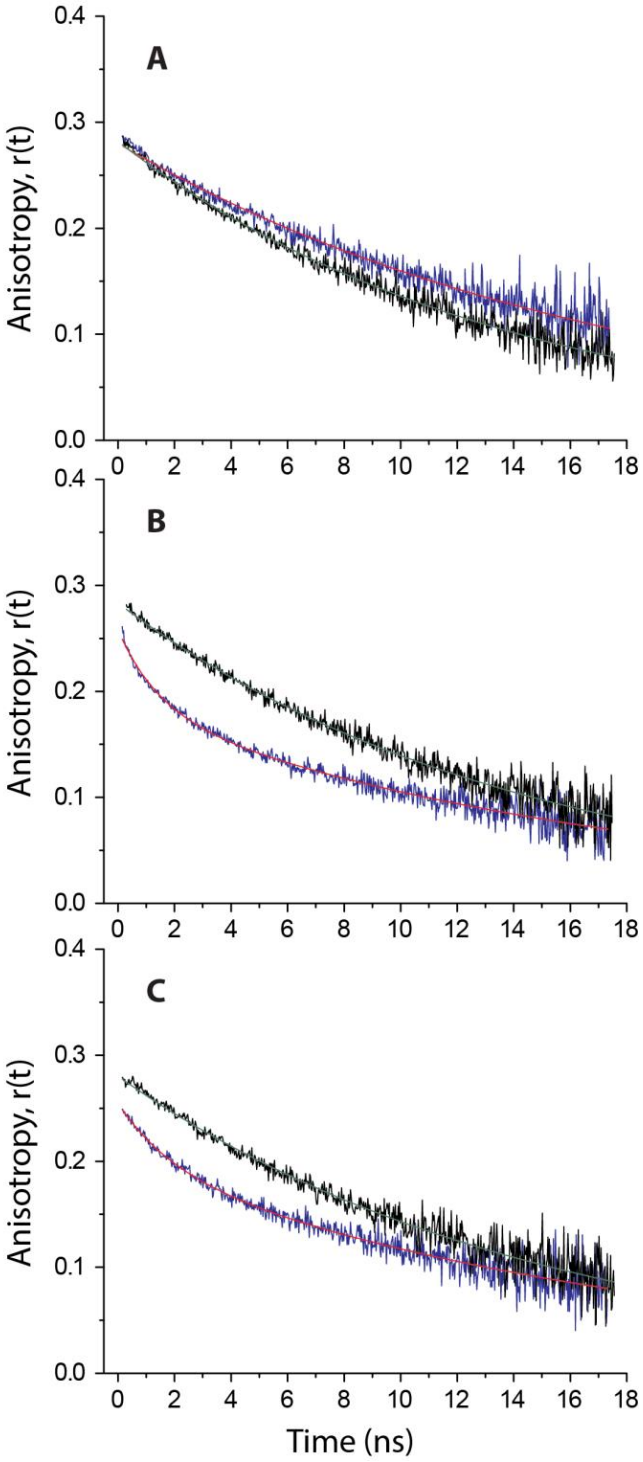

Figure 4.1: One-photon rotational dynamics of the intact (blue curve) and cleaved (black curve) E6 probe is sensitive to both the excitation-detection wavelength and chemical structure as demonstrated using time-resolved anisotropy. Under 425 nm excitation, the anisotropy decays of both the donor (A: 475/50 nm) and acceptor (B: 531/40 nm) were recorded. In addition, both the donor and acceptor were excited at 465 nm (C: 531/40 nm).

The initial anisotropy of all molecules used in this Thesis seems to be smaller than the expected theoretical value (r_0= 0.4), as shown in Table 4.1. Following the conventional interpretation of such deviations, we attribute this difference to the presence of ultrafast non-radiative processes that compete with the excited-state relaxation via fluorescence pathways (75). We used the initial anisotropy values to calculate the angle between the absorbing and emitting dipoles of the intact and cleaved E6 probe (Eq. 2.5). When exciting and detecting the donor, the angle between the dipoles seems to be in agreement for both cleaved (46.3°) and intact E6 (46.6°). However, when exciting donor and detecting acceptor, an increase in angle θ of the intact protein as compared with the cleaved protein was observed. This increase of θ for intact E6 can be explained by the energy transfer that occurs between the photoselected donor and the acceptor whose dipole is more randomly oriented (Table 4.1).

Table 4.1: Fitting parameters of time-resolved anisotropy of intact and cleaved E6 probe as measured using TCSPC technique with emission-polarization analysis according to equation 2.4.

$\lambda_x - \lambda_{fl}$: Probe	β_1	φ_1 (ns)	β_2	φ_2 (ns)	r_0	θ
425 – 475/50:						
Intact E6	—	—	0.280	17.8	0.280	46.6°
Cleaved E6	—	—	0.287	13.3	0.287	46.3°
425 – 531/40:						
Intact E6	0.074	1.47	0.184	18.0	0.258	47.8°
Cleaved E6	—	—	0.283	14.1	0.283	46.5
465 – 531/40:						
Intact E6	0.058	1.95	0.197	19.3	0.255	47.9°
Cleaved E6	—	—	0.280	14.9	0.280	46.6°

Similar measurements were carried out on the other four probes to examine the effects of linker length and flexibility on FRET efficiency. The results are summarized in Figure 4.2 and Table 4.2 as a function of linker length in buffer. Under 425 nm excitation and 531/40 nm detection, our results indicate that the G12 probe with the shortest, most flexible linker exhibits enhanced energy transfer efficiency (36%) with a distinct anisotropy profile. In accordance with our model that attributes the dependence of the fast component to k_{ET}, the G12 probe has the largest fast component contribution. Based on the observed energy transfer efficiency, we calculated the donor-acceptor distance for each construct using the assumption that the absorption and emission spectra remain similar to the construct, GE (Fig 2.1).

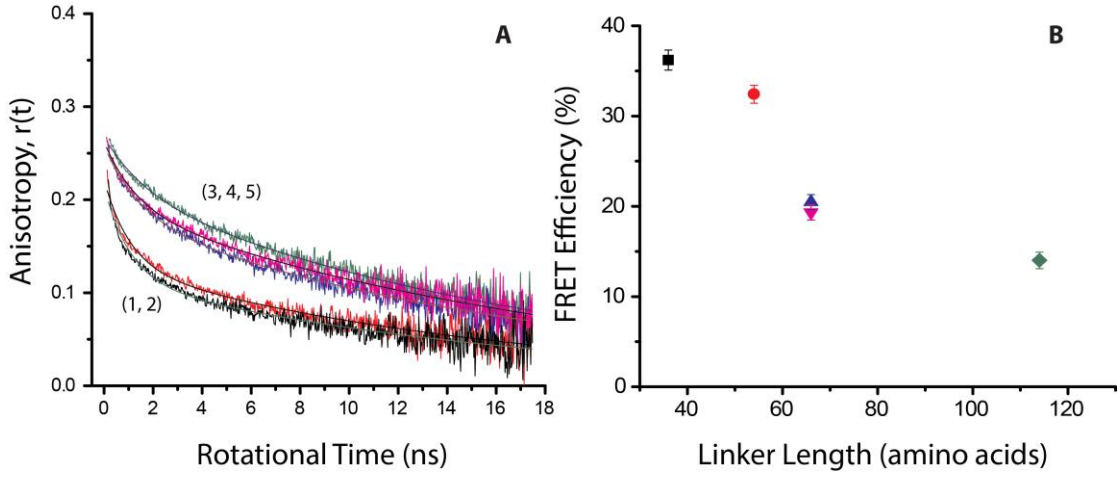

Figure 4.2: Panel A, anisotropy decays of all constructs in phosphate-buffered saline. (black curve 1, G12; red curve 2, G18; blue curve 3, E6; pink curve 4, E6G2; green curve 5, GE. Panel B, FRET efficiencies of all constructs in PBS as a function of linker length based on anisotropy model. The G12 probe with the shortest, most flexible linker exhibits enhanced energy transfer efficiency with a large fast component contribution. Green diamond = GE, pink triangle = E6G2, blue triangle = E6, red circle = G18 and black square = G12. The error displayed is the standard error based on the fitting parameters of a single trial propagated through Eq. 3.2.

The calculated donor-acceptor distance of the five constructs is summarized in Table 4.2 (Eq. 2.3) assuming the Förster distance of the FRET probes with the same donor and acceptor, albeit the linker length, is 5.26 nm in PBS buffer. We observe that as the linker length increases, the estimated donor-acceptor distance also increases. E6 and E6G2, which have the same linker length based on the sequence alone, also exhibit the similar donor-acceptor distance. These results suggest that the linker length is likely the predominant factor that influences the FRET efficiency, rather than the flexibility of the linker. As discussed above, we also observed that as the extent of energy transfer increase, the angle between the absorbing and emitting dipoles becomes greater.

Table 4.2: Fitting parameters of all constructs in PBS under 425 nm excitation and 531/40 nm detection.

$\lambda_x - \lambda_{fl}$: Probe	β_1	φ_1 (ns)	β_2	φ_2 (ns)	r_0	θ	E	R_{DA} (nm)
425 – 531/40:								
GE	0.055	1.70	0.212	18.1	0.267	47.3°	14.0%	7.12
E6G2	0.068	1.28	0.194	18.8	0.262	47.6°	19.3%	6.68
E6	0.074	1.47	0.184	18.0	0.258	47.8°	20.5%	6.60
G18	0.092	1.06	0.129	16.2	0.221	49.7°	32.4%	5.95
G12	0.099	1.06	0.114	16.6	0.213	50.1°	36.2%	5.78

Based on our wavelength-dependent measurements, we conclude that the energy transfer efficiency of the probes can be best estimated using time-resolved anisotropy under 425 nm excitation of the donor and 531/40-nm detection of the donor-acceptor emission. Such conclusions guided our experimental design in the following Chapters concerning the environmental effects on the energy transfer efficiency of the five FRET probes.

4.2.2 Wavelength-dependence of FRET probes rotational dynamics in glycerol-enriched PBS

We carried out wavelength-dependent time-resolved anisotropy of the five FRET constructs as a function of glycerol concentration. As viscosity increases, we hypothesize that the thermal fluctuations (i.e., mobility) observed in buffer will be reduced. Figure 4.3A,B shows representative time-resolved anisotropy decays of intact and cleaved E6, excited at 425 nm and detected at 531/40 nm, as a function of glycerol concentration (0–760 g/L). As described above, the anisotropy of E6 decays as a biexponential in phosphate-buffered saline with a faster decay component of (1.47 ± 0.13) ns ($\beta_1 = 0.074$) and a slower overall rotational time of (18.0 ± 0.4) ns. The fast decay component is attributed to a depolarization mechanism that includes both rotational mobility and energy transfer rate constant (k_{ET}) between the donor and the acceptor. In Figure 4.3, as the glycerol concentration (i.e., bulk viscosity) increases, both the overall slow rotational time and the amplitude fractions of E6 increase. The apparent trend is qualitatively consistent with the Stokes-Einstein model, which predicts that the rotational time of a fluorophore is directly proportional to the viscosity of the surrounding environment. The time constant and amplitude fraction of the FRET-based fast decay component slightly increases with glycerol concentration (Table 4.3).

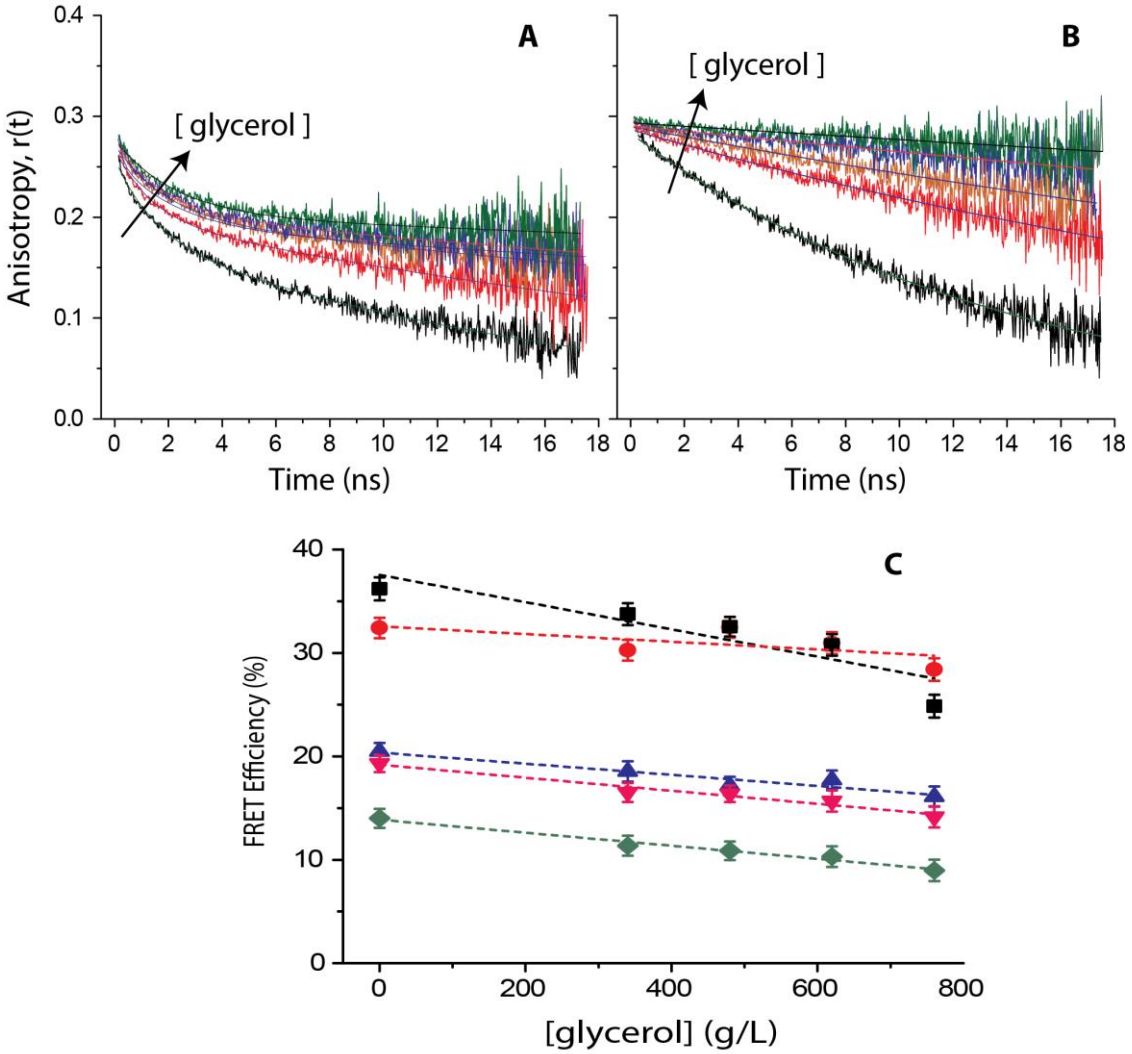

Figure 4.3: Representative rotational dynamics of the intact (panel A) and cleaved (panel B) E6 probe's sensitivity to homogeneous viscosity as demonstrated using time-resolved anisotropy. The colors in A and B represent increasing glycerol concentrations from (0–760 g/L). Under 425 nm excitation and 531/40-nm detection, the anisotropy decays for increasing glycerol concentrations were recorded. Panel C, the corresponding FRET efficiencies of all constructs in glycerol can be seen. Green diamond = GE, pink triangle = E6G2, blue triangle = E6, red circle = G18 and black square = G12. The error displayed is the standard error based on the fitting parameters of a single trial propagated through Eq. 3.2.

According to our model, these results suggest that the energy transfer rate (k_{ET}) and energy transfer efficiency (E%) of E6 decrease slightly as the viscosity of the surrounding environment increases. The observed trend is consistent with the notion that high viscosity would reduce the thermal fluctuation of the dipole moments of both the

donor and acceptor and therefore the sampling of preferred dipole orientations for enhanced FRET. Such trends in homogeneously viscous environments seem independent of the linker length among the FRET probes studied in this Thesis (Fig. 4.3C). These findings are also in general agreement with previous steady-state spectroscopy based studies (51).

Table 4.3: Fitting parameters of time-resolved anisotropy of intact and cleaved E6 probe in glycerol-enriched buffer as measured using TCSPC technique with emission-polarization analysis.

$\lambda_x - \lambda_{fl}$: **425 – 531/40:**	$\boldsymbol{\beta_1}$	$\boldsymbol{\varphi_1}$ **(ns)**	$\boldsymbol{\beta_2}$	$\boldsymbol{\varphi_2}$ **(ns)**	$\boldsymbol{r_0}$	$\boldsymbol{R_{DA}}$ **(nm)**
E6						
340 g/L	0.068	1.32	0.200	35.0	0.269	6.64
480 g/L	0.072	1.90	0.200	64.5	0.272	6.68
620 g/L	0.075	1.74	0.205	91.1	0.269	6.57
760 g/L	0.075	2.23	0.202	183	0.277	6.66
Cleaved E6						
340 g/L	—	—	0.287	37.2	0.287	—
480 g/L	—	—	0.290	57.1	0.290	—
620 g/L	—	—	0.291	108	0.291	—
760 g/L	—	—	0.294	172	0.294	—

A resulting increase in the intermolecular distance between the donor and acceptor is also apparent which supports the reduction in FRET efficiency. This trend is observed with all five FRET probes, indicating a possible stabilization of the extended structure in viscous environments (Figure 4.4).

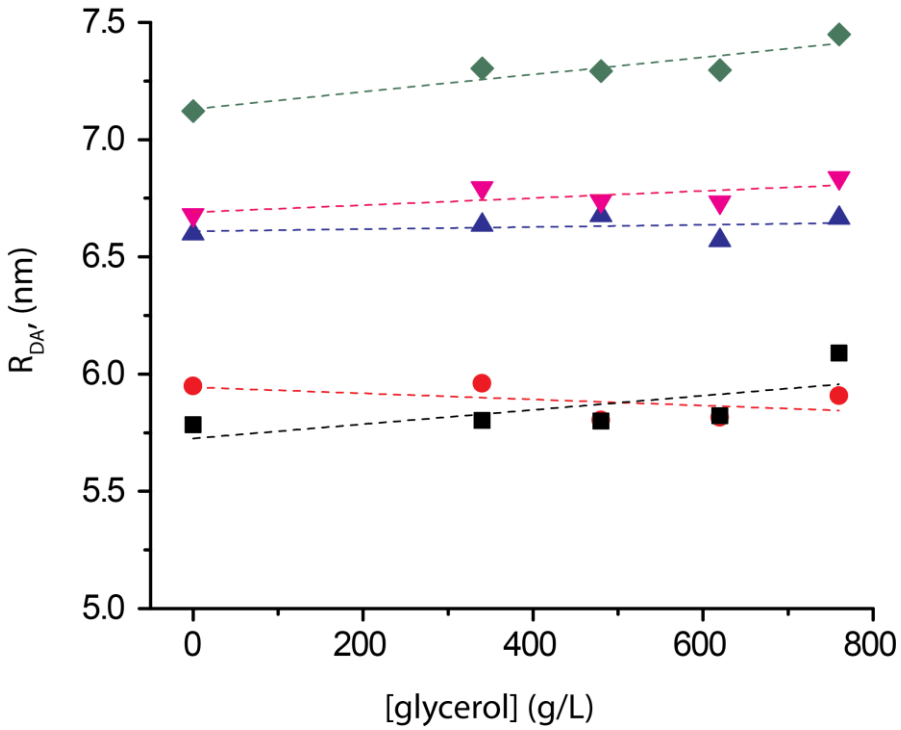

Figure 4.4: Average distance between the donor and acceptor of all probes as a function of glycerol-enriched buffer. Green diamond = GE, pink triangle = E6G2, blue triangle = E6, red circle = G18 and black square = G12. The dotted line indicates the data trend for guidance and not a fit.

4.2.3 Effects of homogenous viscosity on the rotational diffusion coefficient of the FRET probes

We examined the validity of the Stokes-Einstein model in describing the rotational diffusion of flexible hetero-FRET probes in homogeneous environments at room temperature. According to the Stokes-Einstein model, the rotational diffusion of the probes should be linearly proportion to the bulk viscosity of the surrounding environment. Thus, the slow rotational time component in the measured time-resolved anisotropy of each FRET probe was used to calculate the corresponding rotational diffusion rate (D_R). Figure 4.5A shows a representative plot of the rotational diffusion coefficient ratio (D_0 / D_c) *versus* the viscosity ratio (η_c / η_0) of GE and its cleaved counterpart, both excited at 425 nm and detected at 475/50 nm, in glycerol-enriched buffer. This excitation/detection was used because rotation is the only contribution to

fluorescence depolarization. With the exception of the low viscosity range (0–5 cP), our results indicate that the rotational diffusion rate of GE negatively deviates from the Stokes-Einstein model (dotted lines) in glycerol. Similar trends were observed for the other four FRET constructs, including their cleaved counterparts. The observed rotational diffusion rate of hetero-FRET probes studied in this Thesis appears at first glance to be surprising. The known light-induced or pH-induced blinking in GFP mutants (76) takes place on a much longer time scale (100–400 μs) than the rotational time scale (<20 ns). As a result, fluorescence blinking can be ruled out as the underlying mechanism for the observed deviation of the rotational diffusion coefficient from the Stokes-Einstein model.

In the Stokes-Einstein model, the rotational diffusion of a spherical fluorophore is inversely proportional to the bulk viscosity of its environment. In contrast, the donor-linker-acceptor in the FRET probes used here are rather flexible, which is a deviation from the assumed spherical structure in this model. Further, the overall hydrodynamic volume of the E6 probe is relatively large (V_{MW} = 95.4 nm^3) and therefore is likely to rotate on much slower time scales (> 20 ns) as compared with the fluorescence lifetime (3–4 ns). Keep in mind that the fluorescence lifetime is considered the time window during which the rotational diffusion of a fluorophore is monitored. As a result, the accuracy of determining the rotational time using time-resolved anisotropy is likely limited because the rotational time of the protein exceeds the corresponding excited-state lifetime. These two arguments seem reasonable in explaining the observed deviation of the rotational dynamics of our hetero-FRET probes from the Stokes-Einstein model.

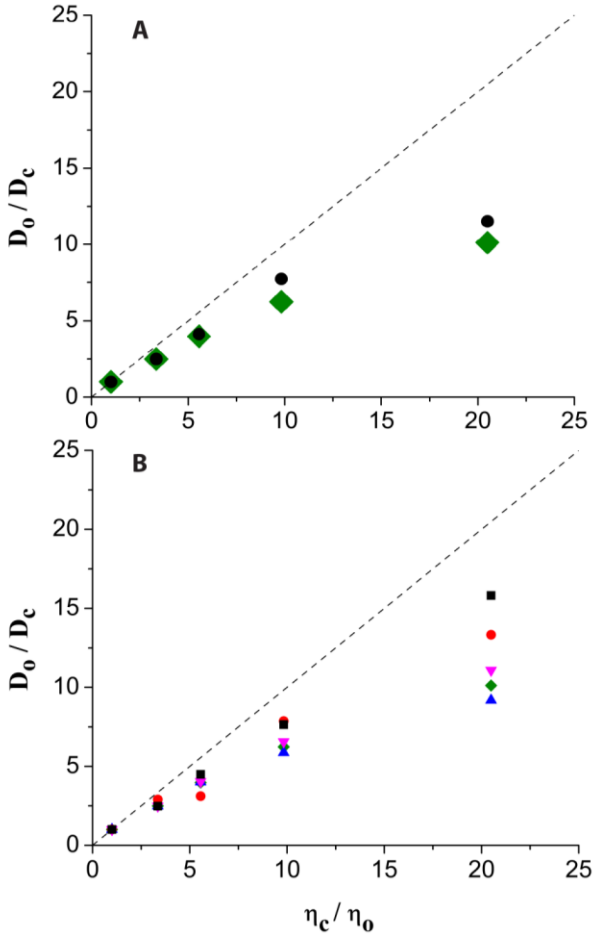

Figure 4.5: Panel A, rotational diffusion ratios of intact (green) and cleaved (black) GE probe as a function of homogenous viscosity under 425 nm excitation and 475/50 nm detection using time-resolved anisotropy. Panel B, rotational diffusion in homogenous viscosity of all constructs. In each environment the probe's diffusion negatively deviates from the Stokes-Einstein model (dashed line). Green diamond = GE, pink triangle = E6G2, blue triangle = E6, red circle = G18 and black square = G12.

Although all of the FRET probes investigated here exhibit negative deviations from the Stokes-Einstein model, we observe in Figure 4.5B that the G12 and G18 probes (black square and red circle, respectively) follow the model more closely. These are the two probes that are the most efficient at energy transfer (Table 4.2, Fig. 4.4). Their more compact structures cause G12 and G18 to be more spherical, allowing them to more closely adhere to the Stokes-Einstein assumption of a spherical shape. In contrast, E6 deviates most from the model suggesting that its rotation may be largely due to local motion of the fluorophore about its linker.

4.2.4 Determining the hydrodynamic volume of FRET probes using steady-state and time-resolved anisotropy

We also used the steady-state anisotropy (Eq. 2.6) and the Perrin-Weber equations, (Eq. 2.7), to independently determine the volume of the rotating moiety of these FRET probes in glycerol-enriched buffer. Figure 4.6A shows that the inverse of steady-state anisotropy of the intact G12 probe is linear with respect to the inverse of the bulk viscosity at room temperature, which is in agreement with Perrin-Weber equation when excited at 425 nm and detected at 475/50 nm. A similar trend was also observed for the cleaved G12 under the same conditions. At this excitation and detection wavelength, only the donor is being monitored, therefore the donor's rotation is the only contribution to the anisotropy decay. According to equation 2.7, the slope of the observed straight line in the Perrin model yields a hydrodynamic volume of 70.9 nm^3 for the intact G12 probe. In contrast, a volume of 62.9 nm^3 was estimated for its cleaved counterpart, which is in general agreement for all five probes (Table 4.4). The similarity of these volumes suggests that the flexibility of the linker in G12 allows the donor to rotate freely.

Table 4.4: Hydrodynamic volumes of intact and cleaved probes under 425 nm excitation and 475/50 detection. The volumes were calculated based on the Perrin-Weber equation (V_{PW}), rotational diffusion (V_{rot}), and the corresponding probe's molecular weight (V_{MW}).

	Intact			**Cleaved**		
$\lambda_x - \lambda_{fl}$: Probe	**V_{PW} (nm^3)**	**V_{rot} (nm^3)**	**V_{MW} (nm^3)**	**V_{PW} (nm^3)**	**V_{rot} (nm^3)**	**V_{MW} (nm^3)**
425 – 475/50:						
GE	90.5	85.5	102	64.6	67.5	43.8
E6G2	85.2	94.3	96.9	64.9	67.4	43.8
E6	84.9	81.9	95.4	65.9	67.4	43.8
G18	75.5	83.5	92.6	63.5	65.0	43.8
G12	70.9	83.2	90.7	62.9	67.6	43.8

To confirm the volume obtained from the Perrin-Weber plot is accurate, we conducted measurements under the same conditions using recombinant cyan fluorescent protein, CFP (BioVision). The free CFP, which is 3.6 kDa larger than the donor, mCerulean3, yielded a volume of 69.1 nm^3 (Figure A3.1). This result confirms that the rotational time measured using time-resolved anisotropy is sensitive to the hydrodynamic volume of the proteins under investigation. Further, the volume calculated from the Perrin equation also increases as the rigidity and length of the linker increases. The cleaved volumes of all five FRET probes are in general agreement with one another, which we would expect because each probe contains the same donor fluorophore.

Using the Stokes-Einstein model and the time-resolved anisotropy of the FRET probes in phosphate-buffer saline, we also calculated the hydrodynamic volume based on the rotational time. In these calculations, we assumed a viscosity of 0.89 cP at room temperature (298 K). The estimated hydrodynamic volumes of the FRET probes investigated here are also summarized in Table 4.4. For the sake of argument, we also used the known molecular weight of the FRET probes to predict its volume based on equation 2.11.

The volumes calculated from the Perrin-Weber equation when exciting and detecting the donor appear to depend on the linker length. The GE probe, which has the longest linker, has the largest corresponding volume. Similarly, the G12 probe with the shortest linker has the smallest volume, which we attribute to its compact, spherical shape. The volume based on rotational diffusion in buffer appears to be more dependent on the structure of the linker rather than the length. Here, we observe that E6G2 has the largest volume (94.3 nm^3) based on the helices connection directly to the fluorophores which restricts its rotation. One would expect G12 and G18 to have the fastest rotation due to the flexibility of the linkers. However, based on the compact nature of these probes, they appear to be rotating slower than the E6 probe based on the volumes calculated in Table 4.4. This indicates that for E6 we observe the rotation of only the donor, yet for G18 and G12 we observe the rotation of the entire probe as one unit.

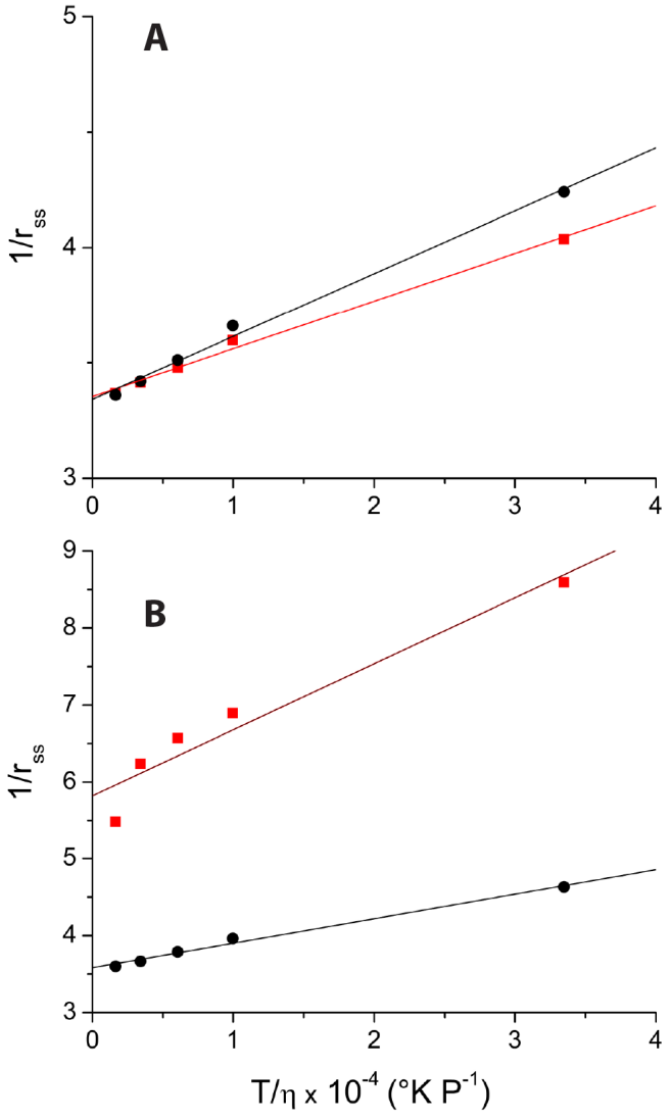

Figure 4.6: Steady-state anisotropy of the G12 probe according to the Perrin-Weber equation in homogenous viscosity. Panel A, under 425 nm excitation and 475/50 nm detection both cleaved (black) and intact (red) obey the Perrin equation. In panel B, the donor was excited at 425 nm and the acceptor was detected at 531/40 nm for both cleaved and intact

Interestingly, when exciting the donor and detecting the acceptor we see that the intact G12 now deviates from the Perrin-Weber equation but cleaved G12 still agrees (Fig 4.6B). This deviation is conventionally attributed to local motion that causes a fast depolarization at low viscosities. However, if local motion was occurring in our FRET probes we would also expect to see deviation when exciting/detecting our donor. Hence,

we attribute this deviation to the rapid depolarization due to FRET. When comparing the five probes we see a correlation between the extent of deviation and the relative FRET efficiency of that probe (Table 4.5). The cleaved acceptor of the five probes are in general agreement and are slightly smaller than the cleaved donor which is to be expected when considering their relative molecular weights of 27 kDa and 27.5 kDa, respectively (Table 4.5).

Table 4.5: Hydrodynamic volumes of intact and cleaved probes under 425 nm excitation and 531/40 detection. The volumes were calculated based on the Perrin-Weber equation (V_{PW}), rotational diffusion (V_{rot}), and the corresponding probe's molecular weight (V_{MW}).

	Intact		**Cleaved**		
$\lambda_x - \lambda_{fl}$: Probe	$\boldsymbol{V_{PW}}$ (nm^3)	$\boldsymbol{V_{rot}}$ (nm^3)	$\boldsymbol{V_{PW}}$ (nm^3)	$\boldsymbol{V_{rot}}$ (nm^3)	$\boldsymbol{V_{MW}}$ (nm^3)
425 – 531/40:					
GE	52.4	83.4	59.5	67.8	43.0
E6G2	46.9	87.0	61.0	68.0	43.0
E6	47.9	76.6	61.0	68.8	43.0
G18	42.2	74.8	59.2	67.5	43.0
G12	34.0	76.6	61.7	67.8	43.0

All of the volumes calculated from the Perrin-Weber equation and the rotational diffusion are smaller than what is predicted based solely upon their molecular weight. This deviation is likely due to the assumption that these proteins are a hard sphere when we calculate their volume based on the molecular weight. Taken together, we speculate that the rotating moiety on the nanosecond time scale, inherent in time-resolved anisotropy measurements, is not necessarily the overall, rigid structure of FRET probes; rather, it is the rotation of a tethered fluorophore due to the flexible linkers.

Chapter 5
Rotational dynamics of confined FRET probes in a crowded environment (Ficoll-70)

Disclosure: This chapter has been published, in part, in the following:

Currie, M.; Leopold, H.; Schwarz, J.; Boersma, A. J.; Sheets, E. D.; Heikal, A. A., Fluorescence dynamics of a FRET probe designed for crowding studies. *The Journal of Physical Chemistry B* **2017,** *121* (23), 5688-5698.

5.1 Background

We carried out similar time-resolved anisotropy measurements on these FRET probes in Ficoll-70-enriched buffer at room temperature as a means to elucidate the heterogeneous viscosity and macromolecular crowding effects on energy transfer efficiency and the rotational dynamics. Ficoll-70 is an inert polymer (70 kDa) and was chosen specifically to minimize weak interactions with the FRET probes, which allows us to understand how the confinement and excluded volumes may influence energy transfer efficiency and the rotational dynamics via steric hindrance. We hypothesize that in a crowded environment, the FRET probes become more compact, which leads to enhanced energy transfer.

5.2 Results and discussion

5.2.1 Rotational dynamics of FRET probes in heterogeneous viscosity

Representative time-resolved anisotropy of E6 as a function of Ficoll-70 concentration is shown in Figure 5.1. These measurements were carried out under 425 nm excitation and 531/40 nm detection, similar to the experiments in glycerol (Chapter 4). Overall, the time-resolved anisotropy exhibits a biexponential decay profile, with a fast and slow component. As the Ficoll-70 concentration increased, the slow rotational time slightly increased, which we would expect based on the Stokes-Einstein model. Unlike glycerol, however, Ficoll-70-enriched buffer is a heterogeneous environment with a mixture of buffer-like regions among excluded volumes that are occupied by the macromolecular crowding agent. In contrast to the slow decay component, the time constant of the fast decay component of the E6 anisotropy decay decreased as the

concentration of Ficoll-70 increased. Additionally, the amplitude fraction of the fast decay increases with increasing Ficoll-70 concentration. Similar trends were observed for the other FRET probes investigated in this Thesis and the results are summarized in Figure 5.1C. The cleaved E6 probe however, decays as a single exponential much like what was observed in glycerol-enriched buffer (Figure 5.1B).

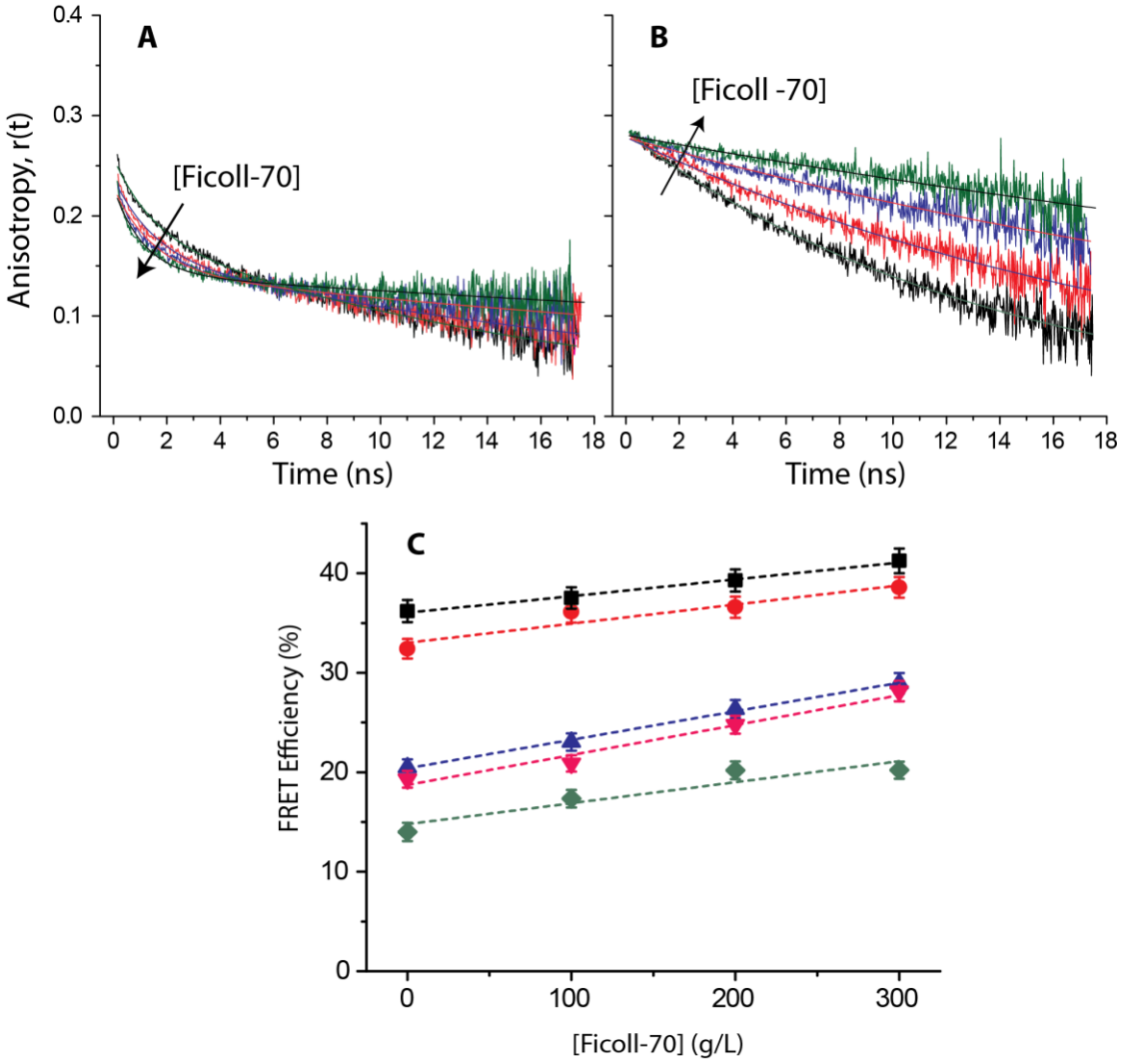

Figure 5.1: Representative rotational dynamics of the intact (panel A) and cleaved (panel B) E6 probe's sensitivity to heterogeneous viscosity as demonstrated using time-resolved anisotropy. The colors in A and B represent increasing Ficoll-70 concentrations from (0–300 g/L).Under 425-nm excitation and 531/40-nm detection, the anisotropy decays for increasing Ficoll-70 concentrations were recorded. Panel C, the corresponding FRET efficiencies of all constructs in Ficoll-70 can be seen. Green diamond = GE, pink triangle = E6G2, blue triangle = E6, red circle = G18 and black square = G12. The error displayed is the standard error based on the fitting parameters of a single trial propagated through Eq. 3.2.

Because the fast decay component is attributed to the energy transfer depolarization mechanism, we may conclude that the energy transfer rate and efficiency increases as the concentration of Ficoll-70 increases (i.e., crowding). An important distinction can be made with our results by comparing homogenous and heterogeneous crowding. In glycerol 620 g/L (~9 cP), E6 has an overall rotational time of 91 ns (Table 4.3). Comparatively, in Ficoll 200 g/L (~10 cP), E6 has an overall rotational time of 49 ns (Table 5.1). Thus, homogenous viscosity seems to have a much greater effect on the mobility of the probes compared to heterogeneous viscosity. This comparison allows us to conclude that excluded volume is what leads to an increase in energy transfer versus viscosity. This conclusion emphasized the capability of the probes to be used to quantify cellular crowding. These observations seem to agree with the general trend reported previously using traditional steady-state spectroscopy (51).

Table 5.1: Fitting parameters of time-resolved anisotropy of intact and cleaved E6 probe in Ficoll-70 as measured using TCSPC technique with emission-polarization analysis.

$\lambda_x - \lambda_{fl}$: 425 – 531/40:	β_1	φ_1 (ns)	β_2	φ_2 (ns)	r_0	θ	R_{DA} (nm)
E6							
100 g/L	0.078	1.57	0.159	26.5	0.238	48.8º	6.40
200 g/L	0.085	1.51	0.144	49.6	0.229	49.3º	6.18
300 g/L	0.086	1.12	0.142	78.2	0.228	49.3º	5.97
Cleaved E6							
100 g/L	—	—	0.278	21.9	0.278	46.7º	—
200 g/L	—	—	0.278	37.4	0.278	46.7º	—
300 g/L	—	—	0.276	48.6	0.276	46.8º	—

Our hypothesis that excluded volume will induce a more compact conformation of the FRET probes is confirmed by our average donor-acceptor distance calculations. In Figure 5.2, we observe that as the concentration of Ficoll-70 increases the distance between the donor and acceptor decreases. This decrease in distance is directly related to the energy transfer rate based on equation 2.3. For the G12 probe, we observe that there is very little change in the donor-acceptor distance due to the already compact structure in buffer. However, when we examine the GE probe that contains a large hinge, we see greater range of distance from buffer to 300 g/L of Ficoll-70.

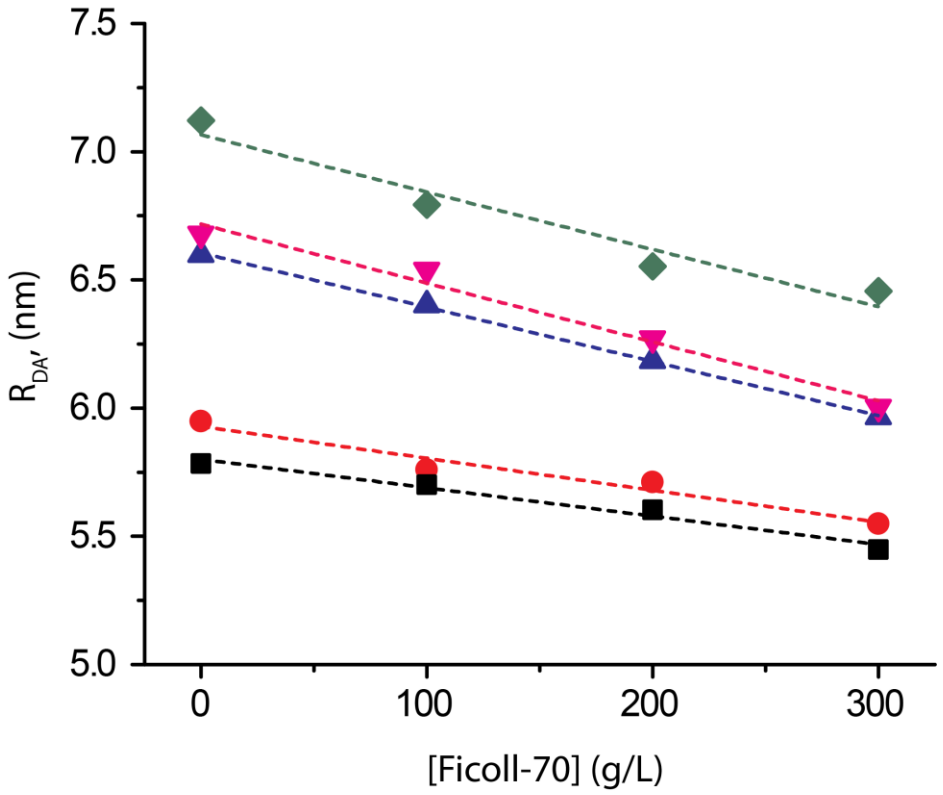

Figure 5.2: Average distance between the donor and acceptor of all probes as a function of Ficoll-70. Green diamond = GE, pink triangle = E6G2, blue triangle = E6, red circle = G18 and black square = G12.

Taken together, our results suggest that time-resolved anisotropy is a viable quantitative approach for determining the energy transfer rate and efficiency of hetero-FRET probes. Importantly, this approach is sensitive to the environment surrounding those probes. These results are the first step to *in vivo* measurements.

5.2.2 Effects of heterogeneous viscosity on the rotational diffusion coefficient of the FRET probes

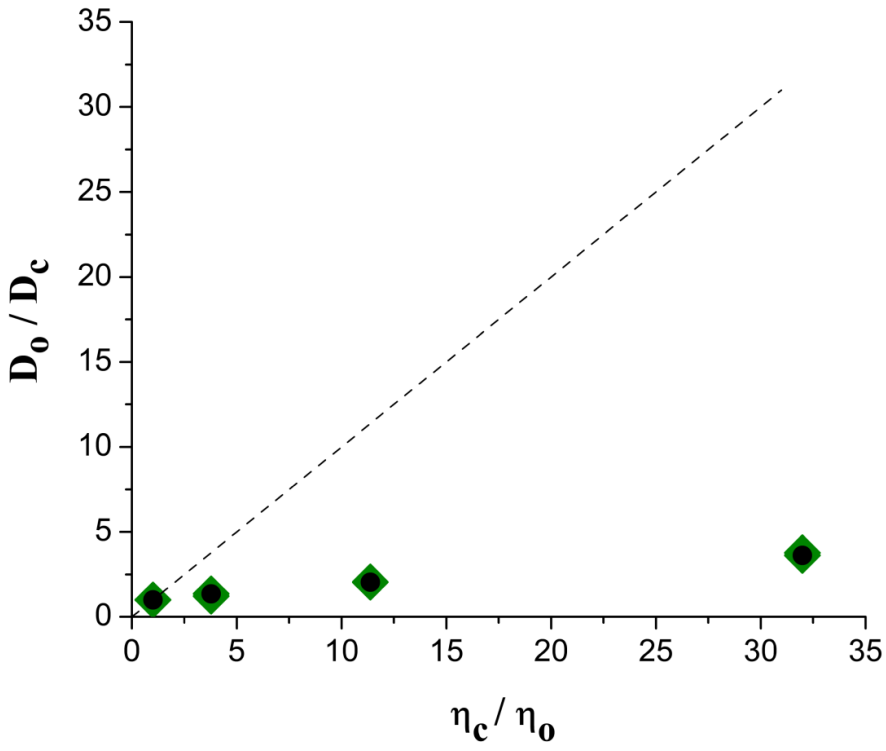

Figure 5.3: Rotational diffusion ratios of intact (green) and cleaved (black) GE probe as a function of heterogeneous viscosity under 425 nm excitation and 475/50 nm detection using time-resolved anisotropy. The dotted line represents what the Stoke-Einstein model predicts.

In homogenous environments, we observed that the GE probe negatively deviated from the Stokes-Einstein model (Fig. 4.5). The GE results reveal even more pronounced deviation from the Stokes-Einstein model when present in Ficoll-enriched environments (Figure 5.3). This enhanced deviation is likely due to the heterogeneous nature of Ficoll-70, which results in microviscosity that is buffer-like compared to the macroviscosity of the solution as a whole.

5.2.3 Effects of heterogeneous viscosity on the Perrin-Weber equation

In Figure 4.6, we showed that both the intact and cleaved G12 probes obey the Perrin-Weber equation we excite and detect the donor. However, in Ficoll-70 enriched buffer the results reveal a deviation from the Perrin-Weber equation, which we again attribute to the heterogeneity of the environmental viscosity (Fig. 5.4A, B). When exciting the donor and detecting the acceptor, we also observe a large increase in the *y*-intercept of intact G12 which corresponds to a small steady-state anisotropy (Figure 5.4B). This indicates a greater extent of depolarization, which can be attributed to the high FRET efficiency of the G12 probe (36.2%). The cleaved, however, has a large steady-state anisotropy corresponding to depolarization only from rotation. Similar results were observed for the intact and cleaved counterpart of the other four probes.

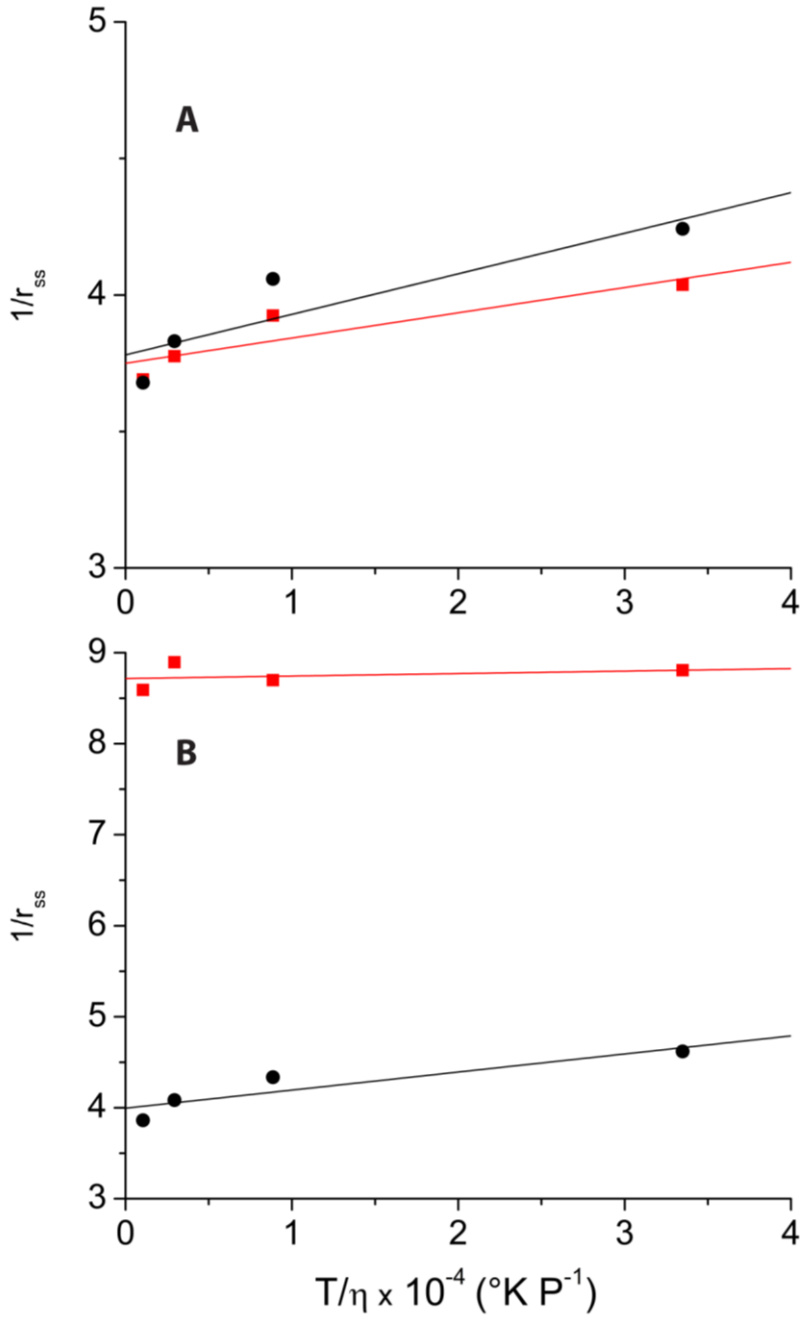

Figure 5.4: Steady-state anisotropy of the G12 probe, following the Perrin-Weber equation in heterogeneous viscosity. Panel A, under 425 nm excitation and 475/50 nm detection both cleaved (black circle) and intact (red square). In panel B, the donor was excited at 425 nm and the acceptor was detected at 531/40 nm for both cleaved and intact.

Chapter 6
Conclusions and future directions

In this Thesis, we investigated the excited-state dynamics of the FRET probes as a function of wavelength for the first time. The rotational dynamics on the nanosecond timescale indicate that the fluorophores are rotating much faster than expected for a 56–64 kDa probe, which we attribute to the flexibility of the linker. Under 425 nm excitation and 531/40 nm detection, we observed a slow and fast component of the anisotropy decay that we attribute to the overall rotation of the probes and energy transfer between the probes, respectively. Using these results, we derived a depolarization model of hetero-FRET to assess the energy transfer efficiency of the probes using time-resolved anisotropy. These energy transfer efficiencies are in general agreement with our efficiencies that are determined from fluorescence lifetime measurements.

Assessment of the FRET efficiencies reveal that the G12 probe which has the shortest most flexible linker has the greatest FRET efficiency (36%) as compared with the GE probe (14%) that has a longer, more rigid linker. In solutions of homogenous viscosity, the FRET efficiency of all five probes decreases due to an increase in the average donor-acceptor distance. This decrease can be explained by the lack of rotational mobility of the fluorophore in a highly viscous environment reducing the potential dipole orientations and possibly stabilizing the extended conformation. However, in heterogeneous environments of similar viscosities imposed by Ficoll-70, the FRET efficiency of all five probes increases with a corresponding decrease in the donor-acceptor distance. This increase in FRET can only be attributed to the excluded volume effects of Ficoll-70, instead of being due simply to viscosity effects which confirms the probes applicability as a sensitive macromolecular crowding sensor.

The hydrodynamic volumes based on the Perrin-Weber equation of the G12 and G18 probes reveal the compact nature of these probes. This compact structure results in enhanced energy transfer efficiencies, which is supported by a smaller donor-acceptor distance. Likewise, as the length and rigidity of the linker increases the subsequent hydrodynamic volume also increases. These measurements indicate the sensitivity of time-resolved anisotropy to reveal the conformational dynamics of the FRET probes.

Now that the effects of viscosity and Ficoll-70 induced excluded volume have been established, experiments exploring different crowding agents will be investigated. The volume fraction of a crowding agent and its shape is known to cause varying types of confinement and crowding effects (52, 77). Therefore, we will explore the size and shape dependence of the macromolecular crowder on the relative conformation and FRET efficiency of the probes using Ficoll-400 and dextrans. It has also been widely accepted that *in vivo* crowding is a combination of both excluded volume and attractive and repulsive forces (38, 39). Future experiments on the probes will mimic these interactions using protein crowders, such as bovine serum albumin and ovalbumin, which are known to exhibit these forces (78, 79). Weak interactions between the fluorescent protein constructs and the protein crowders can be easily distinguished using anisotropy, based on a decrease in the apparent rotation of the probe.

The experiments described in this Thesis focused on measurements in bulk solution. We will begin *in vivo* measurements of macromolecular crowding by transiently expressing these constructs in mammalian cells. To this end, we recently obtained the mammalian expression vectors of these probes. By selectively targeting the FRET probes to specific compartments of a mammalian cell under well-defined cellular conditions, we will be able to quantify the level of crowding as a function of cellular stimuli (e.g., cellular stress or signal transduction) or function (e.g., the cell cycle).

FRET probes have also been obtained that are able to investigate localized changes in ionic strength in bulk solution and live cells. For these probes, there is higher FRET under conditions of lower ionic strength, and the FRET decreases as electrostatic screening occurs. Experiments will first be carried out in bulk solution, analogous to those described here, and then in live cells.

References

1. Ellis, R. J. 2001. Macromolecular crowding: Obvious but underappreciated. Trends Biochem Sci 26:597-604.
2. Minton, A. P. 1992. Confinement as a determinant of macromolecular structure and reactivity. Biophys. J. 63:1090-1100.
3. Minton, A. P., and J. Wilf. 1981. Effect of macromolecular crowding upon the structure and function of an enzyme: Glyceraldehyde-3-phosphate dehydrogenase. Biochemistry 20:4821-4826.
4. Ellis, R. J., and A. P. Minton. 2003. Cell biology: Join the crowd. Nature 425:27-28.
5. Minton, A. P. 1995. Confinement as a determinant of macromolecular structure and reactivity. II. Effects of weakly attractive interactions between confined macrosolutes and confining structures. Biophys. J. 68:1311-1322.
6. Parsegian, V. A., R. P. Rand, and D. C. Rau. 2000. Osmotic stress, crowding, preferential hydration, and binding: A comparison of perspectives. Proceedings of the National Academy of Sciences of the United States of America 97:3987-3992.
7. Ellis, R. J. 2001. Macromolecular crowding: An important but neglected aspect of the intracellular environment. Curr. Opin. Struct. Biol. 11:114-119.
8. Minton, A. P. 2001. The influence of macromolecular crowding and macromolecular confinement on biochemical reactions in physiological media. J Biol Chem 276:10577-10580.
9. Zhou, H. X., G. Rivas, and A. P. Minton. 2008. Macromolecular crowding and confinement: Biochemical, biophysical, and potential physiological consequences. Annu Rev Biophys 37:375-397.
10. Weiss, M. 2014. Crowding, diffusion, and biochemical reactions. Int Rev Cell Mol Biol 307:383-417.
11. Berezhkovskii, A. M., and A. Szabo. 2016. Theory of crowding effects on bimolecular reaction rates. J Phys Chem B 120:5998-6002.
12. Tsao, D., A. P. Minton, and N. V. Dokholyan. 2010. A didactic model of macromolecular crowding effects on protein folding. PLOS ONE 5:e11936.
13. Christiansen, A., Q. Wang, M. S. Cheung, and P. Wittung-Stafshede. 2013. Effects of macromolecular crowding agents on protein folding in vitro and in silico. Biophys Rev 5:137-145.
14. Denesyuk, N. A., and D. Thirumalai. 2013. Entropic stabilization of the folded states of rna due to macromolecular crowding. Biophys Rev 5:225-232.
15. Zhou, H. X. 2013. Influence of crowded cellular environments on protein folding, binding, and oligomerization: Biological consequences and potentials of atomistic modeling. FEBS Lett 587:1053-1061.
16. Zhou, H. X. 2004. Protein folding and binding in confined spaces and in crowded solutions. J Mol Recognit 17:368-375.
17. Ådén, J., and P. Wittung-Stafshede. 2014. Folding of an unfolded protein by macromolecular crowding in vitro. Biochemistry 53:2271-2277.

18. ten Wolde, P. R., and A. Mugler. 2014. Importance of crowding in signaling, genetic, and metabolic networks. Int Rev Cell Mol Biol 307:419-442.
19. Rohwer, J. M., P. W. Postma, B. N. Kholodenko, and H. V. Westerhoff. 1998. Implications of macromolecular crowding for signal transduction and metabolite channeling. Proceedings of the National Academy of Sciences 95:10547-10552.
20. Munishkina, L. A., E. M. Cooper, V. N. Uversky, and A. L. Fink. 2004. The effect of macromolecular crowding on protein aggregation and amyloid fibril formation. J Mol Recognit 17:456-464.
21. Lee, C. F., S. Bird, M. Shaw, L. Jean, and D. J. Vaux. 2012. Combined effects of agitation, macromolecular crowding, and interfaces on amyloidogenesis. J Biol Chem 287:38006-38019.
22. Latshaw, D. C., M. Cheon, and C. K. Hall. 2014. Effects of macromolecular crowding on amyloid beta (16-22) aggregation using coarse-grained simulations. J Phys Chem B 118:13513-13526.
23. Magno, A., A. Caflisch, and R. Pellarin. 2010. Crowding effects on amyloid aggregation kinetics. The Journal of Physical Chemistry Letters 1:3027-3032.
24. Shtilerman, M. D., T. T. Ding, and P. T. Lansbury, Jr. 2002. Molecular crowding accelerates fibrillization of alpha-synuclein: Could an increase in the cytoplasmic protein concentration induce parkinson's disease? Biochemistry 41:3855-3860.
25. McNulty, B. C., G. B. Young, and G. J. Pielak. 2006. Macromolecular crowding in the escherichia coli periplasm maintains α-synuclein disorder. J. Mol. Biol. 355:893-897.
26. Rusinga, F. I., and D. D. Weis. 2017. Soft interactions and volume exclusion by polymeric crowders can stabilize or destabilize transient structure in disordered proteins depending on polymer concentration. Proteins.
27. Li, C., L. M. Charlton, A. Lakkavaram, C. Seagle, G. Wang, G. B. Young, J. M. Macdonald, and G. J. Pielak. 2008. Differential dynamical effects of macromolecular crowding on an intrinsically disordered protein and a globular protein: Implications for in-cell nmr spectroscopy. J Am Chem Soc 130:6310-6311.
28. Smith, S., C. Cianci, and R. Grima. 2017. Macromolecular crowding directs the motion of small molecules inside cells. J R Soc Interface 14.
29. Li, X., and E. L. Mehler. 2006. Simulation of molecular crowding effects on an alzheimer's beta-amyloid peptide. Cell Biochem Biophys 46:123-141.
30. Cho, E. J., and J. S. Kim. 2012. Crowding effects on the formation and maintenance of nuclear bodies: Insights from molecular-dynamics simulations of simple spherical model particles. Biophys J 103:424-433.
31. Wang, Q., A. Zhuravleva, and L. M. Gierasch. 2011. Exploring weak, transient protein–protein interactions in crowded in vivo environments by in-cell nuclear magnetic resonance spectroscopy. Biochemistry 50:9225-9236.
32. Rivas, G., and A. P. Minton. 2016. Macromolecular crowding in vitro, in vivo, and in between. Trends Biochem. Sci. 41:970-981.

33. Homouz, D., L. Stagg, P. Wittung-Stafshede, and M. S. Cheung. 2009. Macromolecular crowding modulates folding mechanism of alpha/beta protein apoflavodoxin. Biophys J 96:671-680.
34. Zhang, D. L., L. J. Wu, J. Chen, and Y. Liang. 2012. Effects of macromolecular crowding on the structural stability of human alpha-lactalbumin. Acta Biochim Biophys Sin (Shanghai) 44:703-711.
35. Hatters, D. M., A. P. Minton, and G. J. Howlett. 2002. Macromolecular crowding accelerates amyloid formation by human apolipoprotein c-ii. J Biol Chem 277:7824-7830.
36. Minton, A. P. 1981. Excluded volume as a determinant of macromolecular structure and reactivity. Biopolymers 20:2093-2120.
37. Michael, S., N. Samantha, V. Franck, D. B. Meredith, and H. Loren. 2017. Effects of soft interactions and bound mobility on diffusion in crowded environments: A model of sticky and slippery obstacles. Physical Biology.
38. Miklos, A. C., C. Li, N. G. Sharaf, and G. J. Pielak. 2010. Volume exclusion and soft interaction effects on protein stability under crowded conditions. Biochemistry 49:6984-6991.
39. Sarkar, M., C. Li, and G. J. Pielak. 2013. Soft interactions and crowding. Biophysical Reviews 5:187-194.
40. Feig, M., I. Yu, P.-H. Wang, G. Nawrocki, and Y. Sugita. 2017. Crowding in cellular environments at an atomistic level from computer simulations. The Journal of Physical Chemistry B.
41. Hall, D., and A. P. Minton. 2003. Macromolecular crowding: Qualitative and semiquantitative successes, quantitative challenges. Biochimica et Biophysica Acta (BBA) - Proteins and Proteomics 1649:127-139.
42. Kim, J. S., and A. Yethiraj. 2011. Crowding effects on protein association: Effect of interactions between crowding agents. J Phys Chem B 115:347-353.
43. Kenworthy, A. K. 2001. Imaging protein-protein interactions using fluorescence resonance energy transfer microscopy. Methods 24:289-296.
44. Biswas, S., and P. K. Chowdhury. 2015. Unusual domain movement in a multidomain protein in the presence of macromolecular crowders. Phys Chem Chem Phys 17:19820-19833.
45. Heyduk, T. 2002. Measuring protein conformational changes by fret/lret. Curr Opin Biotechnol 13:292-296.
46. Ivanov, V., M. Li, and K. Mizuuchi. 2009. Impact of emission anisotropy on fluorescence spectroscopy and fret distance measurements. Biophys J 97:922-929.
47. Stryer, L. 1978. Fluorescence energy transfer as a spectroscopic ruler. Annu Rev Biochem 47:819-846.
48. Lakowicz, J. R. 2006. Principles of fluorescence spectroscopy. Springer US.
49. Förster, T. 1948. Intermolecular energy migration and fluorescence. . Ann. Phys 437:55-75.
50. Wu, P., and L. Brand. 1994. Resonance energy transfer: Methods and applications. Anal Biochem 218:1-13.

51. Boersma, A. J., I. S. Zuhorn, and B. Poolman. 2015. A sensor for quantification of macromolecular crowding in living cells. Nat Meth 12:227-229.
52. Liu, B., C. Aberg, F. J. van Eerden, S. J. Marrink, B. Poolman, and A. J. Boersma. 2017. Design and properties of genetically encoded probes for sensing macromolecular crowding. Biophys J 112:1929-1939.
53. Markwardt, M. L., G.-J. Kremers, C. A. Kraft, K. Ray, P. J. C. Cranfill, K. A. Wilson, R. N. Day, R. M. Wachter, M. W. Davidson, and M. A. Rizzo. 2011. An improved cerulean fluorescent protein with enhanced brightness and reduced reversible photoswitching. PLOS ONE 6:e17896.
54. Laura Marcu, P. M. W. F., Daniel S. Elson. 2014. Fluorescence lifetime spectroscopy and imaging: Principles and applications in biomedical diagnostics. CFC Press.
55. Peter, M., S. M. Ameer-Beg, M. K. Hughes, M. D. Keppler, S. Prag, M. Marsh, B. Vojnovic, and T. Ng. 2005. Multiphoton-flim quantification of the egfp-mrfp1 fret pair for localization of membrane receptor-kinase interactions. Biophys J 88:1224-1237.
56. Duncan, R. R., A. Bergmann, M. A. Cousin, D. K. Apps, and M. J. Shipston. 2004. Multi-dimensional time-correlated single photon counting (tcspc) fluorescence lifetime imaging microscopy (flim) to detect fret in cells. J Microsc 215:1-12.
57. Gopich, I. V., and A. Szabo. 2012. Theory of the energy transfer efficiency and fluorescence lifetime distribution in single-molecule fret. Proceedings of the National Academy of Sciences 109:7747-7752.
58. Tregidgo, C., J. A. Levitt, and K. Suhling. 2008. Effect of refractive index on the fluorescence lifetime of green fluorescent protein. J Biomed Opt 13:031218.
59. Muller, S. M., H. Galliardt, J. Schneider, B. G. Barisas, and T. Seidel. 2013. Quantification of forster resonance energy transfer by monitoring sensitized emission in living plant cells. Front Plant Sci 4:413.
60. Leavesley, S. J., A. L. Britain, L. K. Cichon, V. O. Nikolaev, and T. C. Rich. 2013. Assessing fret using spectral techniques. Cytometry A 83:898-912.
61. Warren, S. C., A. Margineanu, M. Katan, C. Dunsby, and P. M. French. 2015. Homo-fret based biosensors and their application to multiplexed imaging of signalling events in live cells. Int J Mol Sci 16:14695-14716.
62. Zacharias, D. A., J. D. Violin, A. C. Newton, and R. Y. Tsien. 2002. Partitioning of lipid-modified monomeric gfps into membrane microdomains of live cells. Science 296:913-916.
63. Vogel, S. S., T. A. Nguyen, P. S. Blank, and B. W. van der Meer. 2015. An introduction to interpreting time resolved fluorescence anisotropy curves. In Advanced time-correlated single photon counting applications. W. Becker, editor. Springer International Publishing, Cham. 385-406.
64. Demas, J. N. 1983. Chapter 2 methods of measuring lifetimes In Excited state lifetime measurements Academic Press
65. dos Remedios, C. G., and P. D. Moens. 1995. Fluorescence resonance energy transfer spectroscopy is a reliable "ruler" for measuring structural changes in

proteins. Dispelling the problem of the unknown orientation factor. J Struct Biol 115:175-185.
66. Currie, M., H. Leopold, J. Schwarz, A. J. Boersma, E. D. Sheets, and A. A. Heikal. 2017. Fluorescence dynamics of a fret probe designed for crowding studies. The Journal of Physical Chemistry B 121:5688-5698.
67. Ameloot, M., M. vandeVen, A. U. Acuña, and B. Valeur. 2013. Fluorescence anisotropy measurements in solution: Methods and reference materials (iupac technical report). Pure Appl. Chem. 85:589-608.
68. Becker, W. 2005. Advanced time-correlated single photon counting technique. Springer-Verlag Berlin Heidelberg.
69. Berezin, M. Y., and S. Achilefu. 2010. Fluorescence lifetime measurements and biological imaging. Chemical reviews 110:2641-2684.
70. Brilliantov, N. V., V. P. Denisov, and P. L. Krapivsky. 1991. Generalized stokes-einstein-debye relation for charged brownian particles in solution. Physica A 175:293-304.
71. Yengo, C. M., and C. L. Berger. 2010. Fluorescence anisotropy and resonance energy transfer: Powerful tools for measuring real time protein dynamics in a physiological environment. Curr. Opin. Pharmacol. 10:731-737.
72. Xu, Q.-H., S. Wang, D. Korystov, A. Mikhailovsky, G. C. Bazan, D. Moses, and A. J. Heeger. 2005. The fluorescence resonance energy transfer (fret) gate: A time-resolved study. Proceedings of the National Academy of Sciences of the United States of America 102:530-535.
73. Thaler, C., S. V. Koushik, H. L. Puhl, 3rd, P. S. Blank, and S. S. Vogel. 2009. Structural rearrangement of camkiialpha catalytic domains encodes activation. Proc Natl Acad Sci U S A 106:6369-6374.
74. Tramier, M., T. Piolot, I. Gautier, V. Mignotte, J. Coppey, K. Kemnitz, C. Durieux, and M. Coppey-Moisan. 2003. Homo-fret versus hetero-fret to probe homodimers in living cells. Methods Enzymol 360:580-597.
75. Heikal, A. A., S. T. Hess, and W. W. Webb. 2001. Multiphoton molecular spectroscopy and excited-state dynamics of enhanced green fluorescent protein (egfp): Acid–base specificity. Chem. Phys. 274:37-55.
76. Dickson, R. M., A. B. Cubitt, R. Y. Tsien, and W. E. Moerner. 1997. On/off blinking and switching behaviour of single molecules of green fluorescent protein. Nature 388:355-358.
77. Balbo, J., P. Mereghetti, D.-P. Herten, and Rebecca C. Wade. 2013. The shape of protein crowders is a major determinant of protein diffusion. Biophys. J. 104:1576-1584.
78. Ota, C., and K. Takano. 2016. Behavior of bovine serum albumin molecules in molecular crowding environments investigated by raman spectroscopy. Langmuir 32:7372-7382.
79. Wang, Y., C. Li, and G. J. Pielak. 2010. Effects of proteins on protein diffusion. J. Am. Chem. Soc. 132:9392-9397.

Appendix 1: FRET probe purification and proteinase K cleavage.

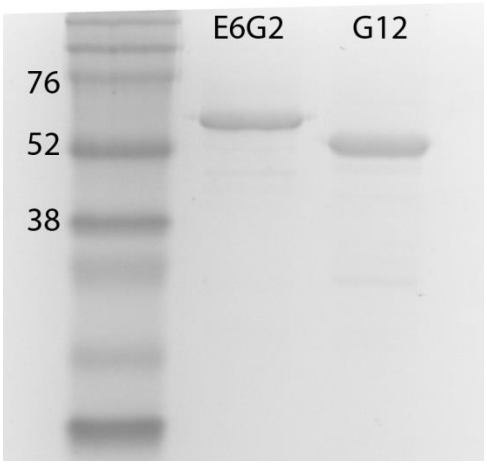

Figure A1.1: Representative 12% SDS-PAGE of purified fractions of intact E6G2 and G12.

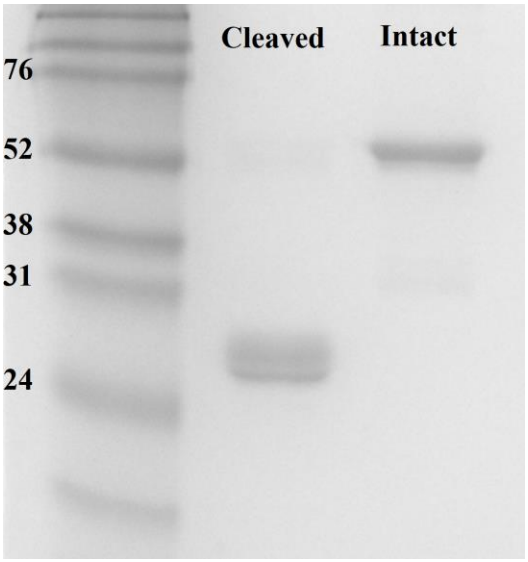

Figure A1.2: Representative proteinase K cleavage of GE construct.

Appendix 2: Bulk viscosity measurements

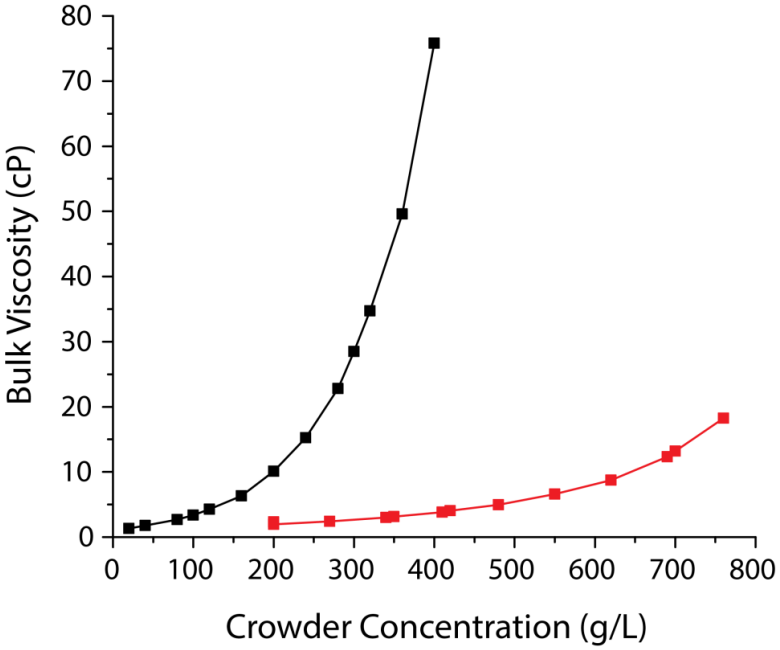

Figure A2.1: Bulk viscosity measured with Ubbelohde viscometers is nonlinearly dependent of the concentration of the crowding agent. Measurements collected by Chang Thao, 2013. Error bars are not shown due to the magnitude being smaller than the markers.

Table A2.1: Viscosity measurements for glycerol and Ficoll-70 including the standard deviation. The viscosity value is an average of three trials. Measurements collected by Chang Thao, 2013.

[crowder] (g/L)	**Viscosity (%)**
glycerol	
340	2.98 ± 0.050
480	4.95 ± 0.015
620	8.75 ± 0.022
760	18.24 ± 0.095
Ficoll-70	
100	3.36 ± 0.003
200	10.12 ± 0.164
300	28.47 ± 0.130

Appendix 3: Additional FRET probe resources

Table A3.1: Förster distance of GE probe collected by Jacob Schwarz, 2016. The standard deviation reported is based on the 30 ps system response of the instrument.

[Environment] (g/L)	R_0 **(nm)**
PBS	5.26
glycerol	
340	5.19
480	5.14
620	5.09
760	5.06
Ficoll-70	
100	5.24
200	5.21
300	5.14

Table A3.2: FRET efficiencies of all probes using fluorescence lifetime measurements collected by Jacob Schwarz, 2016. The standard deviation reported is based on the 30 ps system response of the instrument.

$\lambda_x - \lambda_{fl}$:	E
Probe	(%)
425 – 531/40:	
GE	7.5 ± 0.6
E6G2	10.8 ± 0.6
E6	13.3 ± 0.6
G18	22.2 ± 0.7
G12	24.4 ± 1.0

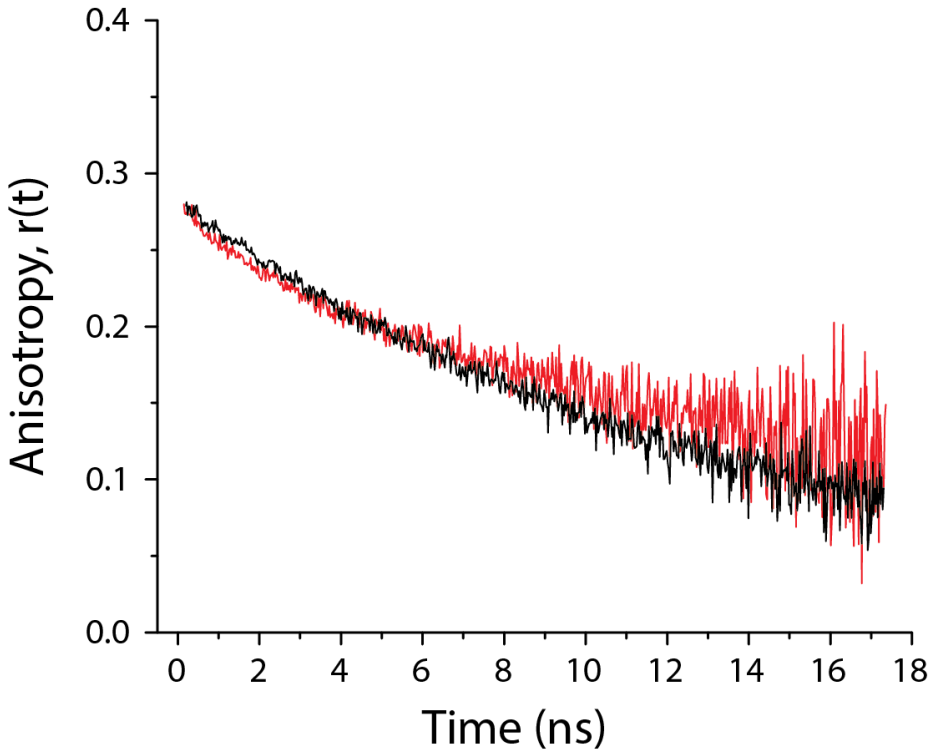

Figure A3.1: Time-resolved anisotropy decay of recombinant CFP (red, 31.1kDa) and cleaved GE (black, 27.5 kDa) in PBS under 425 nm excitation and 475/50 nm detection.